The Ebola virus matrix protein clusters phosphatidylserine, a critical step in viral budding

Monica L. Husby[1,2], Souad Amiar[1,2¶], Laura I. Prugar[3¶], Emily A. David[1&], Caroline B. Plescia[1&], Kathleen E. Huie[3&], Jennifer M. Brannan[3], John M. Dye[3], Elsje Pienaar[2,4], Robert V. Stahelin[1,2*]

[1] Department of Medicinal Chemistry & Molecular Pharmacology, Purdue University, West Lafayette, Indiana, United States of America

[2] Purdue Institute of Inflammation, Immunology and Infectious Disease (PI4D), Purdue University, West Lafayette, Indiana, United States of America

[3] United States Army Medical Research Institute of Infectious Diseases USAMRIID, Fort Detrick, Frederick, Maryland, United States of America

[4] Weldon School of Biomedical Engineering, Purdue University, West Lafayette, Indiana, United States of America

*Corresponding author

E-mail:rstaheli@purdue.edu (RVS)

[¶] These authors contributed equally to this work

[&] These authors also contributed equally to this work

Running title: Targeting PS levels to inhibit EBOV

Keywords: Ebola virus, fendiline, filovirus, matrix protein, phosphatidylserine, plasma membrane, viral budding, VP40

Abstract

Phosphatidylserine (PS) has been shown to be a critical lipid factor in the assembly and spread of numerous lipid enveloped viruses. Here, we describe the ability of the Ebola virus (EBOV) matrix protein eVP40 to induce clustering of PS and promote viral budding *in vitro*, as well as the ability of an FDA approved drug, fendiline, to reduce PS clustering subsequently reducing virus budding and entry. To gain mechanistic insight into fendiline inhibition of EBOV replication, multiple *in vitro* assays were employed including imaging, viral budding and viral entry assays. Fendiline reduced the PS content in mammalian cells and PS in the plasma membrane, reducing the ability of VP40 to form new virus particles. Further, particles that do form from fendiline treated cells have altered particle morphology and decreased infectivity capacity. These complementary studies reveal the mechanism by which filovirus matrix proteins cluster PS to enhance viral assembly, budding, and spread from the host cell while also laying the groundwork for fundamental drug targeting strategies.

23 **Introduction**

24 Ebola virus (EBOV), which was first discovered in 1976, has been of much concern
25 since the unprecedented 2014-16 outbreak in Western Africa (Breman *et al*, 2016). These
26 fears were exacerbated with the 2018-2020 EBOV outbreak in the Democratic Republic
27 of Congo (>2200 fatalities) as well as a small outbreak there in 2021. The FDA approved
28 an EBOV vaccine (efficacy when administered prior to virus exposure) in 2019 and a
29 monoclonal antibody cocktail in 2020 (Graul *et al*, 2020; Mullard 2020); however, the
30 duration and breadth of these outbreaks underscore the dangers of reoccurring outbreaks
31 and the imminent need to develop small molecule counter measures to treat patients who
32 test positive for EBOV. Further, there is still a large gap in knowledge in how EBOV
33 hijacks host cell components to replicate and spread from cell-to-cell, elucidation of which
34 may identify new drug targets.

35 In the Filoviridae family, EBOV and Marburg virus (MARV) are lipid enveloped
36 negative-sense single stranded RNA viruses (Banadyga *et al*, 2016; Mühlberger 2007).
37 One commonly overlooked characteristic of many pathogenic viruses, including EBOV
38 and MARV, is their lipid envelope, which is acquired from the host cell they infect.
39 Furthermore, lipid enveloped negative-strand RNA viruses possess limited viral
40 machinery, often encoding for just a handful of viral proteins. Amongst these viral proteins
41 is the multi-functional matrix protein. These matrix proteins, including the VP40 protein of
42 EBOV (eVP40) and MARV (mVP40), are essential to viral assembly and egress (Stahelin
43 2014; Madara *et al,* 2015). In fact, independent expression of eVP40 or mVP40 leads to
44 the production of virus-like particles (VLPs), nearly indistinguishable from infectious
45 virions (Jasenosky *et al*, 2001; Noda *et al*, 2002; Licata *et al*, 2003). Although these matrix

46 proteins travel through different trafficking pathways within cells, they coalesce at the
47 plasma membrane (PM) to form the viral matrix, which directs viral assembly, budding
48 and the acquisition of their characteristic lipid envelope (Panchal *et al*, 2003; Jasenosky
49 & Kawoaka 2004; Wang *et al*, 2010; Bornholdt *et al*, 2013; Oda *et al*, 2015; Amiar &
50 Stahelin 2020; Wan *et al*, 2020). Importantly, phosphatidylserine (PS) has been
51 implicated in recruiting matrix proteins to the PM and coordinating the assembly of
52 progeny virions (Adu-Gyamfi *et al*, 2015; Wijesinghe & Stahelin 2015; Bobone *et al*, 2017;
53 Del Vecchio *et al*, 2018).

54 While lipids play a critical role in assembly of new viral particles, lipids are also
55 actively involved in viral entry in a phenomenon known as “apoptotic mimicry”. Apoptotic
56 mimicry is central to the efficient entry of numerous lipid-enveloped viruses (Jemielity *et*
57 *al*, 2013; Moller-Tank *et al*, 2013; Carnec *et al*, 2015). During apoptotic mimicry, PS is
58 transferred from the inner to the outer leaflet of the PM; this causes PS to become a
59 component of the outer viral envelope during infection (Adu-Gyamfi *et al*, 2015; Amara &
60 Mercer 2015; Nanbo & Kawoaka 2010). Subsequently, the exposed PS in the viral
61 envelope is recognized by target cell receptors for viral uptake, continuing the viral
62 lifecycle (Kondratowicz *et al*, 2011; Moller-Tank *et al*, 2013; Brunton *et al*, 2019).

63 The two bilayers of the PM have varying compositions of four main phospholipid
64 classes asymmetrically distributed across the two bilayers (Bell *et al*, 1981; Van Meer *et*
65 *al*, 2008). However, the most abundant anionic lipid within the inner leaflet of the PM is
66 PS, a frequent participant in peripheral protein recruitment (Cho & Stahelin 2005; Stahelin
67 *et al*, 2014; Kerr *et al*, 2018). Extensive work has looked at the dynamic nature of lipids
68 within the PM, including PS, and their tendency to cluster into domains several hundred

69 nanometers in size (Fairn *et al*, 2011; Hirama *et al*, 2017; Bobone *et al*, 2017). Clustering
70 of anionic lipids into domains enriches regions of the PM with anionic charge, creating a
71 platform for electrostatic interactions at the PM interface for peripheral protein
72 recruitment. This phenomenon has been reported between PS and the matrix protein of
73 influenza A virus (Bobone *et al*, 2017). Although significant work has underscored the
74 importance of PS in filovirus budding and entry (Moller-Tank *et al*, 2013; Moller-Tank &
75 Maury 2014; Soni & Stahelin 2014; Stahelin 2014; Adu-Gyamfi *et al*, 2015; Del Vecchio
76 *et al*, 2018; Brunton *et al*, 2019), the molecular details of the interaction has not been
77 explored in the context of the lateral organization of PS, matrix assembly or implications
78 on viral spread.

79 The FDA approved drug, fendiline, has been reported to reduce PS levels within
80 the PM inner leaflet (Cho *et al*, 2016; van der Hoeven *et al*, 2018), which was sufficient
81 to inhibit the oncogenic protein K-Ras PM localization and signaling (van der Hoeven *et*
82 *al*, 2013; van der Hoeven *et al*, 2018). Fendiline was initially approved by the FDA in the
83 1970s as a non-selective calcium channel blocker to treat coronary heart disease (Bayer
84 *et al*, 1987); however, these recently identified off target properties were found to be
85 calcium independent and associated with the indirect inhibition of acid sphingomyelinase
86 (ASM) (Cho *et al*, 2016; van der Hoeven *et al*, 2018). eVP40 has been shown to utilize
87 PS for PM localization, assembly, and production of progeny virions (Adu-Gyamfi *et al*,
88 2015; Del Vecchio *et al*, 2018; Johnson *et al*, 2021); however, detailed molecular insight
89 into this relationship is lacking. To delineate the molecular architecture and requirements
90 of PS concentration on VP40 assembly, oligomerization and budding, we employed
91 biochemical and biophysical assays *in vitro* and in cells. We also tested the ability and

92 mechanism by which eVP40 clusters PS *in vitro* and in cells. We hypothesized that
93 reduction of PS from the PM with fendiline treatment would perturb EBOV assembly and
94 inhibit viral budding. Lastly, fendiline treatment was tested as a potential therapy for
95 inhibition of EBOV budding and spread in biosafety level (BSL)-2 and BSL-4 models of
96 infection.
97

98 ## Results

99 **EBOV VP40 localizes to PS enriched regions in synthetic membranes and in living**
100 **cells**

101 eVP40 has been reported to have selectivity and high affinity for PS (Ruigrok *et al*,
102 2000; Scianimanico *et al*, 2000; Adu-Gyamfi *et al*, 2015; Del Vecchio *et al*, 2018) and
103 PI(4,5)P_2 (Johnson *et al*, 2016; Johnson *et al*, 2018), both *in vitro* and in cells. To establish
104 an *in vitro* system for eVP40-PS colocalization, we employed a giant unilamellar vesicle
105 (GUV) system with fluorescently labelled His_6-eVP40 and a fluorescent PS molecule,
106 TopFluor® TMR-PS (tetramethylrhodamine-PS (TMR-PS)).
107 Dipalmitoylphosphatidylserine (DPPS) was chosen for this assay as eVP40 associates
108 with saturated PS containing membranes *in vitro* more significantly than PS mono- or
109 diunsaturated containing membranes (data not shown). In GUVs supplemented with
110 40% DPPS, a homogeneous ring structure of eVP40-Alexa488 surrounding the GUV
111 membrane (Fig EV1A, *middle panel*) was observed and a random plot profile analysis
112 indicated a small overlap of the two fluorescent signals at the membrane (Fig EV1C,
113 indicated by the asterisk). To investigate further the ability of eVP40-Alexa488 to
114 associate with membranes similar to the PM, GUVs containing both 40% DPPS and 2.5%

115 PI(4,5)P_2 were used (Fig EV1A *right panel*)(See Material and Methods section for
116 important temperature preparation guidelines). The plot profile analysis of the image in
117 Expanded View Fig 1A revealed a strong overlap between the two fluorescence signals
118 (eVP40 and TMR-PS) (Fig EV1D). The protein enrichment analysis also supported this
119 previous observation with an enrichment index of ~5.4 ± 2, four times more than
120 membranes devoid of PI(4,5)P_2 (Fig EV1E). These data are in agreement with the
121 previously published findings that eVP40 requires both PS and PI(4,5)P_2 for efficient
122 membrane binding and oligomerization and suggest eVP40 is able to enrich PS at sites
123 of VP40 oligomerization.

124 To expand upon our findings, we investigated if eVP40 localized to PS enriched
125 regions within the plasma membrane of live cells. To visualize PS and protein localization
126 simultaneously, we transiently expressed EGFP-fused proteins in HEK293 cells and
127 supplemented the cells with TMR-PS immediately prior to imaging (Fig EV2A). To test
128 the hypothesis that eVP40 localizes to PS enriched regions of the PM, we examined the
129 plot profile analysis of TMR-PS and eVP40 by expressing functionally unique EGFP fused
130 proteins: WT-eVP40, Lact-C2 (a PS binding reporter), K224A-eVP40 (a PS-binding
131 residue mutant (Del Vecchio *et al*, 2018), and WE/A-eVP40 (oligomerization deficient
132 mutant (Adu-Gyamfi *et al*, 2012; Bornholdt *et al*, 2013). The fluorescence profile of EGFP-
133 WT-eVP40 vs. TMR-PS revealed a strong overlap between the two fluorophores (Fig
134 EV2A,D). This cellular data corroborates our *in vitro* data, demonstrating that EGFP-
135 eVP40 localizes to PS enriched regions of both model membranes and in the PM of cells.
136 Additionally, there was no significant fluorescence signal overlap between the EGFP-
137 K224A-eVP40 mutant and TMR-PS (Fig EV2A,E), which supports the requirement of PS

138 binding for PM localization of eVP40 (Del Vecchio *et al*, 2018). Importantly, random plot
139 profile analysis revealed a moderate overlap in the fluorescence signals of the
140 oligomerization deficient mutant WE/A-eVP40 and TMR-PS (Fig EV2A,F). This is
141 important to note as this protein is still able to interact with PS at the PM, however, is
142 unable to properly oligomerize (Hoenen *et al*, 2010; Adu-Gyamfi *et al*, 2012; Adu-Gyamfi
143 *et al*, 2013). These results suggest VP40 interacts with PS at the PM inner leaflet as a
144 dimer without significant oligomerization, in line with VP40 *in vitro* lipid-binding (Del
145 Vecchio *et al*, 2018).
146

147 **EBOV-VP40 enhances clustering of PS in synthetic membranes and in living cells**

148 Biophysical and molecular studies into PS dynamics in model membranes and
149 living cells revealed that PS basally distributes into clustered domains enriched with PS
150 (Fairn *et al*, 2011; Hirama *et al*; 2017; Bobone *et al*, 2017). Interestingly, cellular proteins
151 such as Annexins are known to significantly enhance the clustering of PS (Menke *et al*,
152 2005) and viral proteins such as M1 of Influenza A virus have a selectivity for these PS
153 clusters (Bobone *et al*, 2017). However, detailed examination of PS clustering and
154 whether filovirus matrix proteins such as eVP40 alter the organization of PS has not yet
155 been explored.

156 Confocal 3D reconstruction of GUVs (with DPPS and PI(4,5)P_2) indicated different
157 structures of TMR-PS clusters observed where eVP40-Alexa488 fluorescence was
158 enriched (Fig EV1A, *three right columns*). Furthermore, the Mander's coefficient index of
159 correlation was quantified (between the TMR-PS and eVP40-Alexa488) with varying lipid
160 compositions (Fig 1B) demonstrating a statistically significant increase in PS clustering

161 when eVP40-Alexa488 was incubated with GUVs containing both DPPS and PI(4,5)P_2
162 (Fig. 1b; *p<0.0001). These results suggest that eVP40 induced PS clustering *in vitro,*
163 which was significantly enhanced in the presence of both PS and PI(4,5)P_2, akin to the
164 lipid composition typically found in the PM inner leaflet.

165 Next, we were interested if eVP40 was able to induce PS clustering in synthetic
166 membranes in the absence of PI(4,5)P_2. Therefore, we performed a TMR self-quenching
167 experiment as described previously (Zhao *et al*, 2010; Wen *et al*, 2018). The TMR
168 fluorescent group has potent self-quenching properties when two molecules or more are
169 brought in close distance from each other. We tested the ability of eVP40 to undergo TMR
170 self-quenching when fluorescent PS was incorporated in lipid vesicles, as a secondary
171 effect to eVP40-induced PS-clustering. We also tested different eVP40 concentrations
172 and different PS ratios to investigate if TMR self-quenching was concentration dependent.
173 The strongest TMR self-quenching in all membranes was observed at 1.5 μM eVP40 (Fig
174 1C). As expected, higher PS molar ratios resulted in stronger eVP40 induction of TMR
175 self-quenching except for a high molar ratio of DPPS (60% molar ratio). However, the
176 addition of PI(4,5)P_2 at 2.5% molar ratio to 60% DPPS-containing membranes rescued
177 TMR self-quenching similarly to 40% DPPS-containing membranes. Further, DPPS-
178 containing membranes at 60% molar ratio with or without PI(4,5)P_2 displayed a maximum
179 of TMR-PS self-quenching at 2 μM eVP40. These observations may indicate a saturation
180 of the liposome membranes with eVP40 at high PS concentrations. Altogether, this assay
181 demonstrated that eVP40 is able to cluster PS, which is enhanced in the presence of
182 PI(4,5)P_2.

183 We next examined if eVP40 enhanced PS clustering in the PM of cells. As
184 previously mentioned, PS selectively localizes into clustered regions (Fairn *et al*, 2011;
185 Hirama *et al*; 2017; Bobone *et al*, 2017); and we were able to detect a basal level of PS
186 enriched clusters in our control GFP expressing cells, with PS clusters accounting for
187 approximately ~8% of the PM (Fig 1D *top panel* and Fig 1E). Our method was further
188 validated by expressing an additional control protein with a glycosylphosphatidylinositol
189 membrane anchor conjugated to GFP (GFP-GPI), which revealed PS clusters in ~8% of
190 the PM area (Fig 1E; Representative image in Fig EV3B *top panel*).

191 We next sought to determine if our technique accurately captured enhanced PS
192 clustering using the established EGFP-Annexin A2 PS reporter (Menke *et al*, 2005). As
193 shown in Fig 1D-E*,* expression of EGFP-Annexin A2 significantly enhanced PS clustering
194 roughly 2-fold, compared to EGFP expressing cells (***p=0.0001). Taken together, these
195 findings corroborate the previously reported effect of Annexin A2 on PS organization
196 (Menke *et al*, 2005), as well as validate the method developed for our assay. In contrast,
197 expression of EGFP-PLCδ-PH (PI(4,5)P_2) or EGFP-LactC2 did not significantly alter the
198 extent of PS clustering (Fig 1E). This confirmed that transient expression of fluorescently
199 conjugated lipid-binding proteins is not sufficient to enhance PS clustering at the PM.

200 Next, we evaluated the effect of eVP40 expression on PS organization across the
201 PM. EGFP-WT-eVP40 increased PS clustering by ~2 fold (*p=0.004), similar to the PS
202 clustering observed with Annexin A2 (Fig 1D,E). However, expression of the PS-binding
203 deficient mutant EGFP-K224A-eVP40 showed no significant change in PS clustering (Fig
204 1D,E), supporting the hypothesis that eVP40 must interact with PS to promote its
205 clustering at the PM. Additionally, to investigate if eVP40 matrix oligomerization was

206 important for PS clustering, we expressed EGFP-WE/A-eVP40 in HEK293 cells. It is
207 important to note that this mutant still colocalizes with PS at the PM (Fig EV2A,F) albeit
208 to a lesser extent than WT (Adu-Gyamfi *et al*, 2012). Although the WE/A-eVP40 and PS
209 interaction is maintained in cells, no significant increase in PS clustering was observed
210 (Fig 1D,E). To the best of our knowledge, this is the first account of a filovirus matrix
211 protein modulating the organization of PS within the PM. Moreover, these results
212 demonstrate that both membrane binding and oligomerization of eVP40 is central to
213 eVP40-mediated PS clustering.
214

215 **eVP40 membrane binding and oligomerization are dependent on**
216 **phosphatidylserine content in lipid membranes**

217 Next, we hypothesized eVP40 may require PS clustering for productive
218 interactions at the PM during assembly. Enrichment of PS within regions of the PM would
219 provide additional PS molecules available to recruit eVP40 to platforms of viral budding.
220 To investigate how increasing the amount of PS within membranes dictates eVP40
221 membrane affinity, surface plasmon resonance (SPR) was performed with His_6-eVP40
222 and large unilamellar vesicles (LUVs) with increasing concentrations of PS (POPC matrix
223 with PS added from 1% to 22 mol% PS; Fig 2A-C). eVP40 displayed moderate binding to
224 LUVs with 1% PS, with an apparent affinity of 2.5 μM (Fig 2A). However, increasing the
225 concentration of PS to 11% increased the apparent affinity of eVP40 to 0.65 μM (Fig 2B).
226 eVP40 displayed even stronger affinity to vesicles with 22% PS, with an apparent affinity
227 (K_d) of ~0.18 μM (Fig 2C). These results indicate that by increasing the amount of PS in
228 membranes, the affinity of eVP40 to lipid membranes can be modulated. This finding

229 supports the hypothesis that PS clustering may be a mechanism for the virus to provide
230 the necessary electrostatic contacts needed for matrix assembly during viral production.
231 Once at the PM, VP40 oligomerizes into the extensive matrix that gives rise to the
232 stability and structure of the virion. Previously, Adu-Gyamfi et al (Adu-Gyamfi *et al*, 2015)
233 highlighted the importance of PS in this process, where a cell line deficient in PS synthesis
234 showed a significant reduction in eVP40 oligomerization. Moreover, our confocal
235 clustering data (Fig 1D,E) revealed that eVP40 oligomerization is crucial for modulating
236 PS organization into clustered domains. To investigate how increasing PS concentration
237 alters eVP40 oligomerization, we utilized chemical crosslinking of His_6-eVP40 which had
238 been incubated with LUVs of increasing PS concentration (Fig 2D,E). Introduction of 15%
239 PS into LUVs led to extensive eVP40 oligomerization beyond dimeric eVP40 compared
240 to when 0% PS LUVs were used (Fig 2D *lane 2*, Fig 1E). We next tested LUVs containing
241 30% and 60% PS and found that eVP40 oligomerization was even more significantly
242 detected than when just 15% PS was used (Fig 2D *lane 3 and lane 4, respectively*, Fig
243 1E). Compared to LUVs with 0% PS, both 30% and 60% PS led to a significant increase
244 in eVP40 oligomerization (*p=0.021 and *p=0.017, respectively). Further, eVP40
245 oligomerization appeared to saturate when 30% PS was included, as increasing PS
246 content to 60% did not increase eVP40 oligomerization (compared to 30% PS). Taken
247 together, these studies suggest a dynamic relationship between PS clustering and eVP40
248 affinity and oligomerization as a critical step in eVP40 assembly.
249

250 **Total cellular and plasma membrane levels of phosphatidylserine are reduced by**
251 **fendiline treatment**

252 A recent study reported an FDA-approved drug, fendiline, inhibited K-Ras PM
253 localization and signaling (Cho *et al*, 2016) and reduced PM PS content in MDCK cells
254 (Cho *et al*, 2016). Therefore, it was our goal to determine if fendiline could also reduce
255 PS levels in the human cell line HEK293, a cell line commonly used in BSL-2 filovirus
256 studies. The initial finding that fendiline reduced PS levels within the PM (40% reduction,
257 IC_{50} ~3uM) was conducted in MDCK cells using thin-layer chromatography (Cho *et al*,
258 2016), therefore it had not been established if this effect was cell-type specific. To address
259 this, we first established fendiline's toxicity in HEK293 cells after 24 and 48 hours of
260 treatment. No significant toxicity was observed in treatments up to 5 μM fendiline (Fig
261 EV4A). To evaluate the effect of fendiline on PS in HEK293 cells, cells were treated with
262 fendiline for 48 hours and lipids were extracted and quantified by liquid chromatography-
263 tandem mass spectrometry (LC-MS/MS). We observed a significant reduction in cellular
264 PS levels compared to DMSO treated cells, after 48 hour treatment with 1 μM fendiline
265 (~18% reduction; *p=0.012) and 5 μM fendiline (~30% reduction; ***p=0.0003) (Fig 3A).
266 Fendiline exhibited no selectivity in reducing different PS species, as 5 μM fendiline
267 reduced long chain (C>38) and saturated PS species nearly equally (Fig EV4B). It is
268 important to note that the effect of fendiline on PS was specific in that fendiline treatment
269 had no significant effect on another anionic phospholipid, phosphatidic acid (Fig EV4C).
270 Therefore, our data supports the reported finding that fendiline reduced total cellular
271 levels of PS, and that the effect is not cell dependent.

272 As PS is an integral anionic component of the PM inner leaflet, we sought to
273 confirm that fendiline treatment also reduced PS levels within the PM in HEK293 cells.
274 PS localization within the PM has been readily studied by expressing EGFP-LactC2 in

275 mammalian cells (Yeung *et al*, 2008; Kay *et al*, 2012). Therefore, HEK293 cells
276 expressing EGFP-LactC2 were imaged at 24 hours (Fig EV4D) and 48 hours (Fig 3B)
277 post-treatment with increasing concentrations of fendiline. Single doses of 500 nM
278 fendiline had no effect on EGFP-LactC2 PM localization at 24 or 48 hours post treatment
279 (Fig EV4E and Fig 3C, respectively). However, we found a ~30% reduction in PM EGFP-
280 LactC2 localization after 24 hours of treatment for both 1 μM (**p=0.0003) and 5 μM
281 fendiline (**p=0.0045) (Fig EV4E). However, a single dose of 1 μM fendiline treatment did
282 not significantly affect Lact-C2 PM localization after 48 hours of treatment (Fig 3C).
283 Conversely, a single dose of 5 μM fendiline significantly reduced Lact-C2 PM localization
284 even at 48 hours post treatment (~30% reduction; **p=0.0031; Fig. 3c), a reduction similar
285 to that observed at 24 hours post treatment.

286 Fendiline has been known to target L-type calcium channels in the T-tubules
287 (invaginations of the plasma membrane) of muscle cells thereby inhibiting calcium
288 movement and acting as a vasodilator (Bayer & Mannhold 1987). However, in a number
289 of non-muscle cell lines, fendiline has been shown to increase calcium levels, including
290 hepatoma cells (Cheng *et al*, 2001), oral cancer cells (Huang *et al*, 2009), PC prostate
291 cancer cells (Jan *et al*, 2001), and canine kidney cells (MDCK) (Jan *et al*, 2000). Fendiline
292 was also specific in the K-Ras inhibitory affect among a number of L-type calcium channel
293 blockers (van der Hoeven *et al*, 2013) strongly suggesting the fendiline mechanism of
294 action is directly linked to PS depletion and not changes in calcium. Fendiline was shown
295 to inhibit ASM (van der Hoeven *et al*, 2015) thereby reducing plasma membrane
296 sphingomyelin, ceramide, PS and cholesterol. Restoration of ASM activity lead to the
297 relocalization of the PS reporter LactC2 to the PM (van der Hoeven et al, 2015). Lastly,

298 studies in HEK293 cells, the major cell line used herein, demonstrated endogenous
299 calcium channel currents could be distinguished from heterologous expression of L-type
300 calcium channels (Berjukow *et al*, 1996).

301 Thus, based upon rigor of prior research the most likely hypothesis is that fendiline
302 inhibits ASM to alter sphingomyelin levels, which are necessary to maintain proper PS
303 levels in the plasma membrane. Recently, fendiline analogs have been developed with
304 nanomolar potency and have been shown to displace ASM, which is membrane bound in
305 acidic lysosomes leading to ASM degradation (Wang *et al*, 2021) While the direct
306 mechanism of PS depletion in the PM is not fully understood, transbilayer communication
307 may take place across the plasma membrane between sphingomyelin levels on the outer
308 leaflet and phosphatidylserine and cholesterol on the inner leaflet (Llorente *et al*, 2013;
309 Skotland & Sandvig 2019).

310

311 **Fendiline reduces PS clustering**

312 Next, we hypothesized that reduced levels of PS within the PM would therefore
313 reduce the degree of PS clustering. To determine if fendiline treatment reduced the
314 degree of PS clustering, we utilized the Number & Brightness technique (N&B). N&B is a
315 quantitative fluorescence microscopy technique that allows one to detect the aggregation
316 state of proteins with pixel resolution in real time (Digman *et al*, 2008). Previously, N&B
317 was used to quantify PS clustering by analyzing the N&B profile of EGFP-LactC2 (Bobone
318 *et al*, 2017). To accurately capture PS clustering at the PM, imaging was performed at a
319 focal plane near the cell surface (Fig EV4F).

320 To evaluate PS clustering, HEK293 cells expressing EGFP-LactC2 were treated
321 with control or fendiline for 48 hours and the EGFP-LactC2 N&B profile was examined
322 (Fig 3D,E). Three different cluster bin sizes were examined, 1—5, 5-10 and >10. The
323 average percentage of pixels in each bin was calculated and plotted (Fig 3E). Within
324 control-treated cells, significant aggregation of EGFP-LactC2 was observed, with 25%
325 present in complexes of 5-10 LactC2 molecules and ~10% in complexes of >10 LactC2
326 molecules (Fig 3D *top panel* and Fig 3E). This corroborates previous work investigating
327 PS clustering, which found EGFP-LactC2 clusters up to 15 molecules in size (Bobone *et*
328 *al*, 2017). Treatment of cells with 5 μM fendiline abolished the presence of EGFP-LactC2
329 complexes (>10 molecules) and significantly reduced the number of complexes of 5-10
330 LactC2 molecules large (from ~8% in DMSO to ~0% in 5 μM fendiline; **p=0.0043) (Fig
331 3D *bottom panel* and Fig 3E). Moreover, there was a significant (~23%) increase in
332 EGFP-LactC2 complexes of ~1-5 molecules in size in cells treated with 5 μM fendiline
333 compared to control treated cells (****p<0.0001) (Fig 3D *bottom panel* and Fig 3E). Taken
334 together, this data suggests that fendiline treatment disrupted large PS-dependent
335 LactC2 complexes which was compensated by an increase in smaller PS-dependent
336 complexes. Therefore, fendiline may possess antiviral properties by disassembling PS
337 enriched regions that would otherwise have been used as platforms for viral assembly.

338 While the mechanism by which fendiline reduces PS clustering is not known, it has
339 been hypothesized that sphingomyelin changes on the outer plasma membrane can alter
340 the distribution of PS in the inner leaflet (Skotland & Sandvig 2019). This is thought to be
341 attributed to the long fatty acid chains of sphingomyelin interacting with the hydrophobic
342 chains of PS, especially that of PS 18:0/18:1 (Skotland & Sandvig 2019), the most

343 predominant PS species in the plasma membrane. The changes in cholesterol in the
344 plasma membrane could also be partially responsible as optimal levels of sphingomyelin
345 are required for maintenance of cholesterol and PS levels in the plasma membrane inner
346 leaflet (Maekawa *et al*, 2016 Sci Rep) and PS is necessary for proper cholesterol
347 distribution across the plasma membrane (Maekawa & Fairn 2015).
348

349 **Fendiline significantly inhibits authentic EBOV replication**

350 To determine if the FDA-approved drug fendiline was able to inhibit authentic
351 filovirus replication and spread, we first established the toxicity of fendiline in Vero E6
352 cells (Fig EV5A) an established model for BSL-4 filovirus studies (Moe *et al*, 1981), and
353 then monitored the efficacy of fendiline at inhibiting EBOV replication in a BSL-4 setting.
354 Vero E6 cells were used to examine filovirus replication 48, 72 and 96-hours post-
355 infection at different multiplicity of infection (MOI) with EBOV (Kikwit) (Fig 4). Following
356 infection, plates were separated into three post-infection treatment groups (day 0, every
357 day dosing (e.d.), or every other day dosing (e.o.d.)).

358 Fendiline was most effective at reducing EBOV infection in vitro at the highest 20
359 μM concentrations in each treatment group with statistically significant inhibition observed
360 for EBOV at each time point and each treatment group (excluding EBOV 48 hours,
361 e.d.)(****$p<0.0001$, **$p<0.0066$) (Fig 4). Percent inhibition was directly affected by timing
362 of treatments following infection. Furthermore, EBOV infection treatment with fendiline
363 e.d. had the highest inhibition on viral spread at each time point for 20 μM fendiline
364 treatments. Cells of the e.o.d. treatments group, which did not receive treatment
365 immediately following infection with virus, had a dramatically reduced degree of inhibition

366 as compared to the day 0 and e.d. treatment groups, both of which received fendiline
367 immediately following viral infection of one hour.
368
369 **Fendiline reduced EBOV-VP40 localization to the plasma membrane**
370 As both EBOV and MARV-VP40 assembly at the PM is in part governed by PS,
371 we first analyzed both EGFP-eVP40 and EGFP-mVP40 PM localization in cells treated
372 with fendiline for 24 or 48 hours. Treatment with 1 μM and 5μM fendiline had no significant
373 effect on eVP40 PM at 24 hours post treatment (Fig EV5B,C); therefore, EGFP-mVP40
374 PM localization was not assessed further at 24 hours. Since no significant change in
375 EGFP-mVP40 PM localization was observed after 48 hours with either 1 μM or 5 μM
376 fendiline treatment (Fig 5A *bottom panel* and Fig 5B), mVP40 was excluded from further
377 experiments. In agreement with our results thus far, 1 μM fendiline did not significantly
378 inhibit EGFP-eVP40 PM localization after 48 hours of treatment (Fig 5A *top panel* and Fig
379 5C). However, treatment with 5 μM fendiline for 48 hours led to a modest reduction in
380 EGFP-eVP40 PM localization (~6% reduction compared to control treated cells; not
381 significant as p=0.08) (Fig 5A *top panel* and Fig 5C). However, the reduction of eVP40
382 PM localization was not robust enough to lead to the observed inhibition of EBOV by
383 fendiline treatment in our BSL-4 studies (Fig 4). One possible explanation is that a
384 limitation of this technique is the inability to differentiate the extent of VP40
385 oligomerization occurring using basic confocal microscopy. Therefore, it is possible that
386 fendiline reduced PS levels within the PM, but not significantly enough to block VP40's
387 ability to bind to the PM.
388 **VP40 oligomerization is significantly reduced by fendiline treatment**

389 PS is also a key factor promoting the self-assembly of VP40 into the matrix layer
390 of the budding virion (Adu-Gyamfi *et al*, 2013; Adu-Gyamfi *et al*, 2015). This self-assembly
391 process has been highlighted in our *in vitro* crosslinking data (Fig 2D,E) as well as
392 previously reported in live cells utilizing the N&B technique (Adu-Gyamfi *et al*, 2012). To
393 assess how fendiline impacted eVP40 oligomerization in cells, we examined the
394 oligomerization profile of EGFP-eVP40 using the previously described N&B (Adu-Gyamfi
395 *et al*, 2012; Adu-Gyamfi *et al*, 2015; Johnson *et al*, 2016) (Fig 5D,E). The crystal structure,
396 biochemical analysis, and recent Cryo-ET of eVP40 at the PM strongly suggests eVP40
397 binds to the PM as a dimer (Bornholdt *et al*, 2013; Del Vecchio *et al*, 2018; Wan *et al*,
398 2020). eVP40 dimers subsequently oligomerize into larger oligomers via CTD-CTD
399 interactions between dimers, leading to the eVP40 matrix layer formation (Wan *et al*,
400 2020). Therefore, for our data to coincide with the current models of eVP40
401 oligomerization, EGFP-eVP40 oligomers were grouped into bins based on multiples of
402 the dimer. Since analyzing eVP40 oligomerization by an increase in every dimer leads
403 to an abundance of data as well as partial overlap in fluorescence signal for each dimer
404 addition, we simplified the data presentation and analysis to different bins of eVP40
405 oligomers (i.e. dimer-hexamer, hexamer-12mer, 12mer-18mer, and >18mer). The
406 average percentage of pixels in each bin was calculated and plotted for HEK293 cells
407 expressing EGFP-eVP40 and treated with either the control or indicated concentration of
408 fendiline for 48 hrs (Fig 5D,E).

409 Large eVP40 oligomeric structures corresponding to each bin size were readily
410 detectable at the PM in control treated cells (Fig 5D *top panel* and Fig 5E), with ~72% of
411 eVP40 found as a dimer-hexamer, ~16% as a hexamer-12mer, ~8% as a 12mer-18mer,

412 and 3% in complexes >18mer. Treatment with 1 μM fendiline led to a ~8% increase in
413 dimeric-hexameric eVP40, and small decreases in the larger oligomeric structures,
414 although no changes were statistically significant (Fig 5D *middle panel* and Fig 5E).
415 However, the oligomeric profile of eVP40 was statistically different when cells were
416 treated with 5 μM fendiline. Following 5 μM fendiline treatment there was a significant
417 increase in eVP40 found in the dimer-hexameric state (~13% increase; **p=0.0035),
418 which was counterbalanced by an equal reduction in the larger oligomeric states (~6%
419 reduction for hexamer-12mer, 5% reduction for 12mer-18mer, and ~3% reduction for
420 eVP40 structures >18mer) (Fig 5D *bottom panel* and Fig 5E). These results support our
421 hypothesis that by reducing PS concentration and therefore the pool of PS available for
422 clustering, eVP40 is unable to properly oligomerize once it traffics and binds to the PM.
423 This, in combination with the modest reduction in eVP40 PM binding following fendiline
424 treatment, may therefore impact the production of viral particles as suggested from our
425 BSL-4 studies.
426

427 **Fendiline reduced VLP production at the plasma membrane**

428 As fendiline reduced VP40 oligomerization, we sought to determine the effect of
429 fendiline treatment on VLP production using functional budding assays. No significant
430 effect on VLP production was observed for cells treated with 0.5 μM or 1 μM fendiline at
431 either 24 (Fig 6A *lane 3,4* and Fig 6B) or 48 hours post-treatment (Fig 6C *lanes 3,4* and
432 Fig 6D). However, treatment with one dose of 5 μM fendiline for 24 hours led to a ~25%
433 reduction in VLP production (Fig 6A *lane 5* and Fig 6B) compared to DMSO treated cells
434 (Fig 6A *lane 2* and Fig 6B). More importantly, this reduction in VLP production was even

435 more robust when monitored at 48 hours post-treatment, with a statistically significant
436 ~60% reduction in the relative budding efficiency of 5 μM fendiline treated cells (*p-
437 0.0260) (Fig 6C *lane 5* and Fig 6D). The reduction in VLPs is supported by our previous
438 findings that a single dose of 5 μM fendiline reduced PS levels, PS clustering and the
439 extent of eVP40 oligomerization at the PM. Therefore, we hypothesize that reduced virus
440 budding is at least partially responsible for fendiline efficacy in authentic EBOV studies
441 (Fig 4).

442 To further investigate the reduction of VLP production in fendiline treated cells, and
443 to determine if there were any observable morphological changes in VLPs, scanning
444 electron microscopy (SEM) experiments were performed (Fig 6E-F). Micrographs of cells
445 expressing FLAG-eVP40 and treated with 5 μM fendiline revealed minimal VLP
446 production at the PM compared to control treated cells (Fig 6F). These findings support
447 the hypothesis that fendiline treatment considerably reduces the production of EBOV
448 VLPs.

449

450 **VLP morphology is altered by fendiline treatment**

451 The structure and stability of filoviruses is derived from the VP40 matrix underlying
452 the lipid envelope of virions. Therefore, we utilized transmission electron microscopy
453 (TEM) of purified VLPs to determine if disturbing matrix assembly and altering the lipid
454 components of the PM with fendiline treatment changed VLP morphology and possibly
455 infectivity (Fig 7A-C). During filoviral entry, surface exposed GP and viral envelope PS
456 interact with the receptor T-cell immunoglobulin receptor-1 (TIM-1) (Moller-Tank *et al*,
457 2013; Brunton *et al*, 2019). To recapitulate entry-competent VLPs (eVLPs), we co-

458 expressed eVP40 with the Ebola virus glycoprotein (eGP). We performed TEM of eVLPs
459 purified from control and 5 μM fendiline treated cells and used ImageJ software to analyze
460 VLP length and diameter (Fig 7A-C). Control eVLPs were heterogenous in length with a
461 mean length of 4.1 μm ± 2.9 (Fig 7A *left panel* and Fig 7B). Control eVLPs diameter also
462 exhibited a level of heterogeneity but had a fairly consistent diameter of 75 nm ± 12.9,
463 which is similar to previous studies of both virions and VLPs (Noda *et al*, 2002; Liu 2014)
464 (Fig 7A *left panel* and Fig 7C). The length and diameter of eVLPs derived from 5 μM
465 fendiline treated cells were significantly less than control eVLPs. Strikingly, fendiline
466 treatment reduced eVLP length by ~35%, from 4.1 μm to 2.7 μm (*p=0.0139) (Fig 7A *right*
467 *panel* and Fig. 7B) and modestly reduced eVLP diameter (*p=0.043) (Fig 7A *right panel*
468 and Fig 7C). To ensure that eVLPs derived from fendiline treated cells were not more
469 susceptible to damage during the purification, circular dichroism thermal melting was
470 performed and no difference in eVLP stability was observed (Appendix Fig S1). Reduced
471 eVLP length and diameter could translate into reduced infectivity (e.g., less PS and less
472 surface area and membrane available to bind TIM-1), therefore we next sought to
473 determine the effect of fendiline on eVLP entry.
474

475 **Fendiline blocks EBOV eVLP entry**

476 A common characteristic of viral infectivity is the relationship between virion
477 associated PS and the TIM-1 receptor on target cells (Kondratowicz *et al*, 2011; Moller-
478 Tank *et al*, 2013; Wang *et al*, 2017; Dejarnac *et al*, 2018; Brunton *et al*, 2019). Moreover,
479 it has been previously reported that other ASM inhibitors blocked EBOV infectivity (Miller
480 *et al*, 2012). To determine if fendiline treatment reduced the entry of eVLPs, we performed

481 a fluorescent based entry assay using 1,1'-dioctadecyl-3,3,3',3'-
482 tetramethylindocarbocyanine perchlorate (DiI) labelled eVLPs (Nanbo *et al*, 2010; Kuroda
483 *et al*, 2015; Nanbo *et al*, 2019). By testing entry of eVLPs derived from fendiline treated
484 cells rather than the entry of eVLPs on fendiline treated cells, we were able to determine
485 how fendiline treatment affected eVLP entry rather than how inhibition of ASM in target
486 cells affected eVLP entry (as previously described (Miller *et al*, 2012). If entry of the eVLPs
487 was not altered by fendiline treatment, one would expect a dose-dependent increase in
488 infectivity with increasing TIM-1 expression. Conversely, if eVLP entry was inhibited by
489 fendiline treatment, a dose-dependent increase in eVLP entry would not be observed with
490 increasing TIM-1 expression.

491 TIM-1 overexpression was increased in target cells and a detectable and
492 significant dose-dependent increase in control eVLP entry was observed, by more than
493 200% in the highest TIM-1 overexpressing cells (compared to no TIM-1 overexpression;
494 Fig 7D *top panel* and Fig 7E). Remarkably, no measurable increase in eVLP entry was
495 observed for fendiline derived-VLPs across any of the TIM-1 overexpressing target cell
496 conditions (Fig 7D *bottom panel* and 7E). From this comparison, these results suggest
497 that the impaired entry of fendiline eVLPs is a result of reduced PS in the viral envelope,
498 either from smaller VLPs or a lower % of PS content. These findings in combination with
499 the observed reduction in VLP formation further substantiate the significant reduction of
500 EBOV infection observed in our live virus studies following fendiline treatment.

501

502 **Mathematical model of in vitro experiments**

503 We next used a mathematical model to predict how the effects of fendiline on both
504 viral budding and entry combine to produce the observed effects in the BSL-4 assays.
505 We calibrated our mathematical model (equations 1-3) to experimental data from the
506 budding, entry and cellular infection assays using approaches and parameter settings
507 outlined in the methods and Table 1. Results from our two-phase calibration procedure
508 are shown in Fig 8A-F and Appendix Fig S2. The model captures key features of the data
509 including a progressive increase in percentage of infected cells over time, differences
510 between MOI as well as limited cell death in the first 48 hours of the experiment (Appendix
511 Fig S2).

512 The dynamics behind these calibrated figures suggested that fendiline treatment
513 significantly delayed the infection process (Fig 8G,H), resulting in the observed decrease
514 in percent infected cells with treatment over 4 days. The effects of fendiline on budding
515 and entry are estimated to have similar pharmacodynamics (PD), with entry effects
516 estimated to have a slightly stronger response (lower C_{50} and higher E_{max}) compared to
517 budding (Table 1). Based on PD parameters, the response to fendiline was estimated to
518 be weaker in the BSL-4 assays, as is evident by higher C_{50} values and lower E_{max} values
519 compared to the budding and entry assays (Table 1, Fig 8I). These PD parameter
520 differences between budding and entry assays vs BSL-4 results could suggest that other
521 parts of the viral life cycle not affected by fendiline (not quantified explicitly in these
522 experiments) become rate limiting in the BSL-4 assays, thereby reducing the overall effect
523 of fendiline on infection progression. In summary, a mathematical model consistent with
524 three independent experimental systems, predicts a combination of budding and entry

525 effects resulting in the observed BSL-4 effects, and estimates PD parameters for each
526 mechanism.
527

528 ## Discussion

529 The host cell PM is exploited by filoviruses for their assembly and budding, where
530 they can egress the host cell to form a new virion. The matrix protein, VP40, is the main
531 driver of this process as it harbors a high affinity for lipids in the PM inner leaflet. Lipid
532 binding by VP40, which includes selectivity for PS (Ruigrok *et al*, 2000; Scianimanico *et*
533 *al*, 2000; Adu-Gyamfi *et al*, 2015; Del Vecchio *et al*, 2018) and PI(4,5)P_2 (Johnson *et al*,
534 2016; Johnson *et al*, 2018) drives and stabilizes, respectively, VP40 oligomers that are
535 necessary for viral budding. In fact, VP40 has been shown to be sufficient (in the absence
536 of other filovirus proteins) to form VLPs from the host cell PM that are nearly
537 indistinguishable from virions (Jasenosky *et al*, 2001; Noda *et al*, 2002; Licata *et al*, 2004).
538 Again, this underscores the unique properties of VP40 structure and sequence, which
539 provides a template for host lipid binding, oligomerization, and sufficient information to
540 encode cues for scission to complete the viral budding process. Further, VP40 derived
541 VLPs enter cells in a PS-dependent manner despite the absence of the EBOV
542 glycoprotein (Jemielity *et al*, 2013). While some of the basic principles between VP40 and
543 PM interactions have been previously revealed, the mechanistic consequences of the
544 interactions and their potential pharmacological targeting have remained unknown.

545 In this study, we demonstrated that VP40 was able to cluster PS *in vitro* and in the
546 PM of cells. VP40-dependent PS clustering required PS binding and efficient PM
547 localization of VP40, as the K224A-VP40 mutant, previously defined as a PS-binding

548 residue did not significantly increase PS clustering. VP40 oligomerization was also crucial
549 to PS clustering efficiency as a VP40 oligomerization deficient mutant, which can still
550 exhibit PM localization, significantly reduced PS clustering. This is an important point as
551 the PM of host cells is generally thought to harbor 20-30 mol% PS in the inner leaflet. In
552 fact, VP40 effectively binds and oligomerizes on PS-containing membranes with
553 compositions close to the PS-content of the PM inner leaflet. In contrast, PS
554 concentrations below 15 mol% didn't provide robust affinity and oligomerization compared
555 to those with 22 mol% PS and greater. PS clustering and PS content may also play a
556 critical role in the loss of asymmetry that occurs during the EBOV budding process. For
557 instance, pooling of PS in distinct regions of VP40 assembly may provide a cue for
558 scramblases shown to distribute PS to the outer leaflet of the PM during the viral budding
559 process (Nanbo *et al*, 2010; Younan *et al*, 2018).

560 A recent study demonstrated that silencing PSS1, an enzyme responsible for PS
561 synthesis in mammalian cells was sufficient to inhibit EBOV replication (Younan *et al*,
562 2018). However, to the best of our knowledge, small molecules aimed at targeting host
563 cell lipid distribution have not previously been tested against EBOV. Fendiline was a
564 logical choice to form an initial hypothesis of an FDA-approved drug that could inhibit
565 EBOV budding as it was recently shown to lower PM PS (Cho *et al*, 2016) and inhibit K-
566 Ras signaling (van der Hoeven *et al*, 2013; van der Hoeven *et al*, 2018) suggesting this
567 FDA-approved drug may be sufficient to inhibit EBOV budding. Indeed, in BSL-4
568 experiments, fendiline was able to inhibit EBOV replication >75% at 20 μM when given
569 every day post-infection. Follow up mechanistic studies demonstrated that fendiline
570 efficacy was due to inhibition of VP40 oligomerization, viral budding and viral entry. Thus,

571 fendiline, which reduced the PS content of HEK293 cells by ~30%, subsequently reduced
572 PS clustering and VP40 oligomerization necessary for efficient viral budding. VLPs that
573 did form from fendiline-treated cells had an overall reduced length and surface area,
574 which likely combined with the reduced PS-content of the virus or VLPs to limit
575 subsequent viral entry. Thus, disruption of PM PS content by one small molecule was
576 sufficient to effect at least three important steps in the filovirus life cycle. Importantly, an
577 increase in intracellular calcium due to fendiline can be ruled out in reducing and/or
578 inhibiting EBOV and VP40 budding as calcium has been shown to be a critical component
579 of VLP formation and virus replication (Han Z *et al*, 2015). Thus, an increase of calcium
580 in HEK293 cells would be expected to increase and not decrease budding as we've
581 observed.

582 Overall, this study lends credence to the hypothesis that host processes may be
583 targeted to inhibit viral replication and spread. While the potency of fendiline may be low,
584 the combination of fendiline with other FDA-approved drugs that have shown efficacy
585 against EBOV (Johansen *et al*, 2013; Johansen *et al*, 2015; Nelson *et al*, 2016; Dyall *et*
586 *al*, 2018; Jasenosky *et al*, 2019) hold further promise. Fendiline was effective at 5 μM for
587 reducing PS content in cells and the relationship to fendiline concentrations used *in vivo*
588 is an important point to address in the future. Fendiline has been used in both single
589 (200-1200 mg) and multiple doses (400 mg, twice) per day, which was followed with
590 pharmacokinetic evaluation yielding maximal plasma levels in patients of 9-170 ng/mL
591 (Weyhenmeyer *et al*, 1987). At the upper range of fendiline detected in the plasma, 170
592 ng/mL = 540 nM fendiline. Thus, at the upper value of fendiline detected from oral dosing,
593 the concentration was lower than the 5 μM used to lower cellular PS. Part of the issue in

594 fendiline dosing is rapid metabolism with a bioavailability of ~20% depending on the mg
595 dose given (Kurovetz *et al*, 1982). Thus, the issue isn't necessarily fendiline toxicity and
596 efficacy but drug metabolism of fendiline in the plasma and through the hepatic 1st pass
597 effect that limit plasma concentration available (Kurovetz *et al*, 1982). Thus, future
598 studies geared towards more stable drugs that can alter PS content through a similar
599 mechanism of action (via ASM inhibition) may be beneficial.

600 Recently, fendiline analogs have been generated that have nanomolar potencies
601 against K-Ras PS-dependent plasma membrane localization and were effective at
602 inhibiting cancer cell proliferation in the low micromolar range (Wang *et al*, 2021).
603 Fendiline has also been shown to block SARS-CoV-2 S-mediated fusion (Xiao *et al*, 2020)
604 and cause *Leishmania infantum* death via mitochondrial depolarization (Reimão *et al*,
605 2016). Thus, our work and these studies lay a framework to improved pharmacological
606 targeting strategies against either VP40 matrix assembly or PS clustering that would not
607 only reduce viral budding and spread, but lower subsequent viral entry, which partially
608 relies on PS in the viral envelope (Moller-Tank *et al*, 2013; Jemielity *et al*, 2013; Moller-
609 Tank *et al*, 2014; Brunton *et al*, 2019). Notwithstanding pharmacological principles
610 learned from this study, a critical balance between VP40 and PS has been resolved
611 demonstrating a critical need for VP40 clustering in the assembly and budding process.
612 VP40 oligomers are needed for enhanced PS clustering where PS clustering seems to
613 ensure optimal VP40 oligomerization.

614

615 ## Material and Methods

616 ### Reagents & solutions

617 PBS, DMEM, ionomycin and Lipofectamine™ LTX with Plus™ Reagent, and
618 Invitrogen™ Molecular Probes™ Hoechst 3342 were purchased from Fisher Scientific,
619 heat-inactivated fetal bovine serum (FBS) was purchased from Hyclone, and Minimum
620 Essential Medium (MEM) was purchased from Corning. Invitrogen Live Cell Imaging
621 Solution, DiI Stain, Halt™ Protease Inhibitor Cocktail, Pierce BCA Assay kit, and BS3
622 were purchased from ThermoFisher Scientific. Non-essential amino acids (NEAA) were
623 purchased from Sigma Aldrich and L-glutamine was purchased from Gibco. Alexa Fluor™
624 488 C_5 Maleimide (Alexa-488) for protein conjugation was purchased from Invitrogen.
625 Fendiline was purchased from Cayman Chemical Company, prepared in DMSO and
626 stored at -20 °C. Ultra-Pure Grade DMSO was purchased from VWR and the Ni-NTA
627 slurry was purchased from Qiagen. L1 chips for SPR experiments were purchased from
628 GE Healthcare. For cell viability assays, CellTiter-Glo® was purchased from Promega.
629 Antibody information for immunoblotting and immunofluorescence can be found in Table
630 2. Ten percent neutral buffered formalin was purchased from Val Tech Diagnostics
631 (Brackenridge, PA). Cell staining buffer was purchased from BioLegend. stain was
632 purchased from Fisher Scientific.
633

634 **Plasmids**

635 EGFP, EGFP-eVP40 and EGFP-WE/A-eVP40 were prepared as described
636 previously (Adu-Gyamfi *et al*, 2012; Johnson *et al*, 2016). GFP-K224A-eVP40 was
637 prepared by site directed mutagenesis (Johnson *et al*, 2018) GFP-mVP40 was used as
638 described previously (Wijesinghe & Stahelin 2015; Amiar *et al*, 2021). The GFP-LactC2
639 plasmid was a kind gift from Sergio Grinstein (University of Toronto). GFP-PLCδPH was

640 a kind gift from Tamas Balla (NIH). pCAG-GPI-GFP was a gift from Anna Katerina
641 Hadjantonakis (Addgene #32601). pEGFP-N3-Annexin A2 was a gift from Volker Gerke
642 & Ursula Rescher (Addgene #10796). pCAGGS-FLAG-eVP40 (NR49337) and
643 pcDNA3.1-eGP (NR-19814) were obtained from BEI Services. pCAGGS-TIM-1 was from
644 Heinz Feldmann (Watt *et al*, 2014).
645

646 **Lipids and LUV preparation**

647 POPC (#850457), DPPC (#850355), cholesterol (#700000), DPPS (#840037),
648 POPE (#850757), POPS (#840034), Brain PI(4,5)P_2 (#840046), and TopFluor® TMR-PS
649 (#810242) were purchased from Avanti Polar Lipids, Inc. (Alabaster, AL) and stored in
650 chloroform and/or methanol at -20°C until use.. For large unilamellar vesicle (LUV)
651 preparation used in SPR and chemical crosslinking experiments, lipid mixtures were
652 prepared at the indicated compositions (using a POPC matrix as the background and
653 control and the indicated additions of PS at the expense of POPC), dried down to lipid
654 films under a continuous stream of N_2, and stored at -20°C until further use. On each day
655 of experiments, LUVs were brought to room temperature, hydrated in either SPR buffer
656 (10 mM HEPES, 150 mM NaCl, pH 7.4) or chemical crosslinking buffer (260 μM Raffinose
657 pentahydrate in PBS, pH 7.4), vortexed vigorously, and extruded through a 100 nm (SPR
658 experiments) or 200 nm (chemical crosslinking experiments) filter. Vesicle size was
659 confirmed by dynamic light scattering using a DelsaNano S Particle Analyzer (Beckman
660 Coulter, Brea, CA).
661

662 **Preparation and imaging of GUVs**

663 GUVs were prepared by a gentle hydration method (Reeves *et al*, 1969; Darszon
664 *et al*, 1980; Yamashita *et al*, 2002). Briefly, 1 mM of lipid control mixture was made and
665 contained 1,2-dipalmitoyl-sn-glycero-3-phosphocholine (DPPC), cholesterol (Chol) and
666 fluorescent phosphatidylserine (TopFluor® TMR-PS) at 90:9.8:0.2% molar ratio. For PS
667 clustering and eVP40 binding analysis, 1,2-dipalmitoyl-sn-glycero-3-phosphoserine
668 (DPPS) alone or with brain phosphatidylinositol 4,5-bisphosphate PI(4,5)P_2 were added
669 at 40 and 2.5% molar ratios, respectively, and the ratios of DPPC were adjusted
670 accordingly. The lipid mixtures were prepared in 5 mL round-bottom glass flasks and the
671 chloroform was removed with rotary movements under a continuous stream of N_2 and
672 even heat at 55°C until complete evaporation of the solvent. The lipid films were then
673 hydrated overnight at 50°C (DPPC:Chol:TopFluor TMR-PS) and 55°C
674 (DPPC:Chol:DPPS:PI(4.5)P_2:TopFluor TMR-PS) in an appropriate volume of GUV
675 hydration buffer (150 mM NaCl, 10 mM HEPES, 0.5 M sucrose, pH 7.4).

676 For imaging, the freshly hydrated GUVs were diluted 10 times in GUV dilution
677 buffer (150 mM NaCl, 10 mM HEPES, 0.5 M glucose, pH 7.4) and placed on a 6-mm
678 diameter chamber made from a silicon sheet using a core sampling tool (EMS # 69039-
679 60). The silicon chamber was mounted on a 1.5-mm clean coverglass (EMS # 72200-31)
680 pre-coated with 1 mg/mL BSA. The set up was then assembled in an Attofluor chamber
681 (Invitrogen # A7816) and 1.25 μM eVP40-Alexa488 was added. GUVs imaged for eVP40
682 and PS colocalization and clustering analysis was performed at 37°C on a Nikon Eclipse
683 Ti Confocal inverted microscope (Nikon Instruments, Japan), using a Plan Apochromat
684 60x 1.4 numerical aperture oil objective and a 100x 1.45 numerical aperture oil objective,
685 respectively. A 488 nm argon laser was used to excite GFP and a 561 nm argon laser

686 was used to excite TopFluor®-TMR-PS. The 3D reconstruction was performed using
687 ImageJ. Mander's correlational analysis was performed using the plugin JACoP (Bolte &
688 Cordelières 2006).
689

690 **Cell culture, transfections, pharmacological treatments**

691 All BSL-2 studies were performed using HEK293 cells obtained from the American
692 Type Culture Collection and cultured in DMEM supplemented with 10% FBS and 1% PS.
693 Transient transfections were performed using Lipofectamine™ LTX + PLUS™ Reagent,
694 according to the manufacturer's protocol. All transfections were performed in DMEM
695 supplemented with 10% FBS. Treatment with fendiline (in DMSO) occurred at 5-hours
696 post-transfection in DMEM supplemented with 10% FBS. BSL-4 assays were also
697 performed using Vero E6 cells cultured in MEM, 5% heat-inactivated fetal bovine serum,
698 1% L-glutamine, and 1% NEAA. Both HEK293 and Vero E6 cells were cultured and
699 incubated at 37°C, 5% CO_2, 80% humidity.
700

701 **Immunoblotting**

702 Samples prepared for western blotting analysis were first separated using SDS-
703 PAGE (8% for chemical crosslinking and 12% for cell lysates and VLPs). Following
704 transfer onto a nitrocellulose membrane, membranes were blocked with 5% MILK-TBST
705 and analyzed with their respective antibodies (See Table 2). Antibodies were detected
706 using an ECL detection reagent and imaged on the ImageQuant LAS 4000 or Amersham
707 Imager 600 (GE Healthcare Life Sciences). All quantitative analysis derived from western
708 blotting was performed using densitometry analysis in ImageJ.

709

710 **Protein purification and Alexa-488 C_5 Maleimide labelling**

711 The His_6-eVP40-pET46 expression vector was a kind gift from Erica Ollmann
712 Saphire (La Jolla Institute for Immunology) and was expressed and grown in Rosetta™ 2
713 BL21 DE3 competent cells (Merck Millipore, Billerica MA). The pet28a-His_6-Lact C2
714 bacterial expression plasmid was a kind gift from Dr. Sergio Grinstein. His_6-eVP40 and
715 His_6-LactC2 were grown and purified as described previously (Johnson *et al*, 2016).
716 Following elution from a Ni-NTA slurry (Qiagen), the protein samples were then further
717 purified using size exclusion chromatography on a HiLoad 16/600 Superdex 200 pg
718 column (ÄKTA pure, GE Healthcare). The desired fractions containing dimeric VP40 or
719 monomeric LactC2 were collected, concentrated and stored in 10 mM Tris, 300 mM NaCl,
720 pH 8.0. Protein concentration was calculated using the Pierce BCA assay and the protein
721 was stored at 4°C for no longer than 14 days.

722 Labeling of eVP40 cysteine residues was carried out using Alexa-488- C_5-
723 maleimide. eVP40 dimer was treated with a 1.5-fold molar excess of Alexa-488-C5-
724 maleimide dissolved in DMSO for 2 hours at room temperature in maleimide labelling
725 buffer (20 mM NaPi solution pH 7.4, 150 mM NaCl, 4 M Guanidine HCl). The labeling
726 reaction was quenched by adding diothiothreitol (final concentration of 50 mM) and the
727 labeled protein was separated from the non-conjugated dye on a HiLoad 16/600
728 Superdex 200 pg column. Fractions containing eVP40 dimer were collected and
729 concentrated. The labelling efficiency and protein concentration were estimated using a
730 NanoDrop according to Invitrogen's instructions.

731

732 **Plasma membrane localization confocal microscopy**

733 Live cell imaging experiments were performed at 24 hours and 48 hours post
734 treatment. Experiments to quantify fluorescent protein PM localization were performed on
735 a Zeiss LSM 710 inverted microscope using a Plan Apochromat 63x 1.4 numerical
736 aperture oil objective. A 488 nm argon laser was used to excite GFP/EGFP. GFP-LactC2
737 PM localization was quantified ratiometrically by comparing the PM signal vs. the cytosolic
738 signal. GFP-EBOV-VP40 PM localization was quantified ratiometrically by comparing the
739 PM signal vs. the total fluorescence signal within the cell.

740

741 **TMR-PS quenching experiment**

742 The Top Fluor TMR quenching analysis was performed as described previously
743 (Zhao *et al*, 2010). Briefly, LUVs with 0.5% TopFluor® TMR-PS and increasing amounts
744 of DPPS (0, 1, 5, 10, 20, 40, 60%) with or without PI(4.5)P_2 (2.5% with 60% DPPS) were
745 made as described above. LUVs were then mixed at a final concentration of 40 μM with
746 corresponding concentrations of eVP40 dimer in 10 mM HEPES, 160 mM NaCl pH 7.4 in
747 a black/clear bottom 96-well plate and incubated at 37°C for 30 min. The Top Fluor TMR
748 was excited at 547 nm and the fluorescence was recorded from 555 to 600 nm with no
749 cutoff wavelength using the plate reader SpectraMax M5e (Molecular Devices, St Jose,
750 CA). The fluorescence quenching ratio, ΔF, was calculated according to the ratio (F_0/F),
751 where F_0 is the fluorescence in absence of protein and F is the fluorescence at a given
752 eVP40 concentration.

753

754 **Cellular Top Fluor TMR-PS clustering confocal microscopy**

755 Each experimental day, a 100 μM working stock of TopFluor® TMR-PS in
756 methanol was prepared. Immediately prior to imaging, cells were placed in 4°C for 5 min.
757 The working stock was diluted to a final 500 nM TopFluor® TMR-PS solution in 3 mg/mL
758 BSA/PBS. The 500 nM TopFluor® TMR-PS/BSA/PBS solution was incubated with cells
759 at 4°C for 10 min, rinsed three times with cold PBS, and immediately imaged in fresh cold
760 PBS. Top Fluor TMR was excited at 560 nm and GFP was excited at 488 nm. For PS
761 clustering analysis, a custom macro in ImageJ was used. Prior to the macro analysis,
762 background was subtracted and the contrast was enhanced. To isolate the PM area, a
763 default threshold was applied. To isolate PS clusters the Moments analysis thresholding
764 (Tsai 1985) was applied. Following the moments analysis thresholding, the custom
765 ImageJ macro was applied: despeckle, close-, fill holes, and remove outliers (radius=5,
766 threshold=50). The sum of the remaining particles area was calculated, as well as the PM
767 area. %PS clustering was calculated according to the ratio ($Area_{clusters}/Area_{plasma\ membrane}$).

768 **Number & Brightness**

769 Number & Brightness experiments were performed as described previously (Adu-
770 Gyamfi *et al*, 2017; Bobone *et al*, 2017; Johnson *et al*, 2018) on a Zeiss LSM 880 upright
771 microscope using a LD "C-Apochromat" 40x/1.1 W Corr M27 objective. HEK293 cells
772 expressing either GFP, GFP-LactC2 or GFP-eVP40 were treated with fendiline (1 or 5
773 μM) for 48-hours prior to N&B analysis. Cells were imaged in phenol-free live cell imaging
774 solution. For each experimental day, the brightness value of a monomer was determined
775 in cells expressing monomeric GFP. Each image was acquired using the same laser
776 power (0.01), resolution (256x256), pixel dwell time (16 us), frames (50), and zoom (pixel

777 size of 50 nm). SimFCS Globals Software (Laboratory for Fluorescence Dynamics,
778 University of California, Irvine, CA) was used for analysis.
779

780 **Chemical crosslinking**

781 His_6-eVP40 and His_6-LactC2 were purified as previously described in *Protein*
782 *Purification*. LUVs containing POPC and Brain $PI(4,5)P_2$ (2.5%) with varying PS mol%
783 composition (0, 15,30, 60%) were prepared as previously described in *Lipids & Vesicle*
784 *Preparation*. Experimental protocol was adapted from (Johnson *et al*, 2016), and the
785 manufacturers protocol for BS^3 (ThermoFisher) with each step performed at RT. In brief,
786 protein (final concentration of 0.3 μM in PBS pH 7.4) was mixed with LUVs (final
787 concentration = 660 μM) at a 1:1 volumetric ratio for 30 min. Protein bound LUVs were
788 separated from unbound protein through centrifugation (75,000 x *g*, 30 min, 22°C), and
789 resuspended in PBS (pH 7.4) buffer containing BS^3 (final concentration of 200 μM).
790 Samples were incubated for 45 min, quenched with glycine for 15 min and then analyzed
791 through western blotting. Following immunoblotting, oligomerization of VP40 was
792 quantified ratiometrically by comparing $VP40_o$ vs. $VP40_{m+d}$ (where $VP40_o$ is the oligomeric
793 VP40 band density (>75 kDa) and $VP40_{m+d}$ is the sum of monomeric and dimeric eVP40
794 (~37 and 74 kDa) band density).
795

796 **Surface plasmon resonance**

797 To determine the affinity of His_6-eVP40 to LUVs with increasing PS concentrations,
798 SPR was performed. SPR experiments were performed at 25°C using a Biacore X100 as
799 described previously (Adu-Gyamfi *et al*, 2015). In brief, an L1 chip was coated at 5 μL/min

800 with LUVs containing 0% PS (100% POPC, PS added at the expense of POPC) on flow
801 cell 1 and either 1%, 11% or 22 mol% POPS on flow cell 2 (LUV preparation described in
802 previous section, *Lipids and Vesicle Preparation)*. The LUV conjugated chip was
803 stabilized by washing with 50 mM NaOH and blocked with 0.1 mg/mL BSA (in SPR buffer)
804 at a flow rate of 10 µL/min until the response on each flow cell was <100 response units
805 (RU). For quantitative affinity analysis, each concentration of eVP40 was injected for 540
806 s at a flow rate of 10 µL/min with a 180 s delay, and the difference in response between
807 flow cell 1 and flow cell 2 was recorded (ΔRU). The apparent K_d of vesicle binding was
808 determined using the non-linear least squares analysis: $Req = Rmax/(1 +$
809 $\frac{Kd}{C})$where R_{eq} (measured in RU) is plotted against protein concentration (C). R_{max} is the
810 theoretical maximum RU response and K_d is the apparent membrane affinity. Data were
811 fit using the Kaleidagraph fit parameter of (m0*m1)/(m0+m2);m1=1100;m2=1. ΔRU data
812 was normalized in GraphPad Prism 8 for windows (La Jolla, CA) and plotted in
813 Kaleidagraph (Reading, PA).
814

815 **Lipidomics**

816 HEK293 cells were treated with the indicated concentration of fendiline for 48
817 hours, collected through centrifugation, rinsed with PBS and protein concentration was
818 determined. Cells were pelleted, flash frozen in liquid N_2 and stored at -80°C until
819 subsequent LC/MS/MS processing by Avanti Polar Lipids, Inc.. Prior to LC-MS/MS
820 analysis, lipids were extracted using the Folch method (Folch *et al*, 1957). The bottom
821 chloroform layer taken after centrifugation was diluted with internal standards for LPA,
822 LPS, PA and PS for quantization by injection on LC-MS/MS. Samples were injected on a

823 LC-MS/MS method using a Waters Acquity UPLC / AB Sciex 5500 MS system performing
824 reversed phase separation of LPA and LPS and PA and PS components with MS/MS
825 detection. Each molecular species identified by the [M-H] m/z of its acyl carbon:double
826 bond (CC:DB i.e. 34:2 PA) was quantified against the response of the internal standards
827 of known concentration. Content of individual and total LPA/PA and LPS/PS was
828 reported. Values were corrected to $1x10^6$ cells for all samples.
829

830 **BSL-4 immunofluorescence assay**

831 Vero E6 cells were seeded at 2e4 cells/well in black 96-well poly-D-lysine treated
832 plates (Greiner Bio-One Cellcoat®). Twenty-four hours prior to infection, fendiline was
833 diluted in 0.5% DMSO and Vero E6 cell culture media at indicated concentrations and
834 added to cells. An equivalent percentage of DMSO in culture media served as the vehicle
835 control. Following pretreatment, compound was removed, and cells were incubated with
836 Ebola virus (Kikwit) at a multiplicity of infection (MOI) of 0.1 or 1.0 in a BSL-4 located at
837 USAMRIID. Following absorption for 1 hour, virus inoculum was removed and cells were
838 washed. Plates were divided into three post-infection treatment groups (day 0, every day-
839 e.d., every other day-e.o.d.), and received either culture media or freshly prepared
840 fendiline or vehicle control. Cells were then treated daily with freshly prepared compound
841 or left to incubate based on their designated treatment group. At 48 hours (MOI=1.0), 72
842 or 96 hours (MOI=0.1) post infection, cells were washed with PBS and submerged in 10%
843 neutral buffered formalin for 24 hours prior to removal from the BSL-4 laboratory. Formalin
844 was removed and cells were washed with PBS. Cells were blocked with 3% BSA/PBS
845 cell staining buffer (BioLegend) and incubated at 37°C for 2 hours. Ebola virus GP-

846 specific mAb KZ52, diluted in 3% BSA/PBS, was added to appropriate wells containing
847 infected cells and incubated at room temperature for 2 hours. Cells were washed three
848 times with PBS prior to addition of goat anti-human or goat anti-mouse IgG-Alexa-488
849 secondary antibody. Following 1-hour incubation with secondary antibody, cells were
850 washed 3 times prior to counterstaining with Hoechst's stain diluted in PBS. Cells were
851 imaged and percent of virus infected cells calculated using the Operetta High Content
852 Imaging System and Harmony® High Content Imaging and Analysis Software
853 (PerkinElmer).
854
855 **VLP collections & functional budding assays**
856 HEK293 cells were transfected and treated with fendiline as described in the
857 previous section, *Cell Culture, Transfection & Pharmacological Treatments*. Budding
858 assays were performed as described previously (Johnson *et al*, 2016; Harty 2018). In
859 brief, VLP containing supernatants were harvested from cells and clarified through low
860 speed centrifugation. Clarified VLPs were loaded onto a 20% sucrose cushion in STE
861 buffer (10 mM TRIS, 100 mM NaCl, 1 mM EDTA, pH 7.6), isolated through
862 ultracentrifugation, and resuspended in either 150 mM ammonium bicarbonate (functional
863 budding assays), 2.5% glutaraldehyde in 0.1 M cacodylate buffer (TEM experiments),
864 STE buffer (entry assays) or 0.1 M phosphate buffer for CD and thermal melting (PB; 0.02
865 M sodium phosphate monobasic, 0.08 M sodium phosphate dibasic, pH 7.4). VLP
866 samples were stored at -80°C for functional budding assays, -20°C for entry assays or
867 4°C for TEM and CD analysis.

868 For functional budding assays, cell lysate samples were harvested and lysed on
869 ice with RIPA buffer (150mM NaCl, 5mM EDTA pH=8, 50mM Tris pH 7.4, 1% Triton-X,
870 0.1% SDS, 0.5% deoxycholic acid) supplemented with Halt™ Protease Inhibitor Cocktail.
871 Prior to separation on a 12% SDS-PAGE gel, cell lysate and VLP sample volume loading
872 were normalized to sample protein content, determined by a BCA assay. Gels were
873 transferred to a nitrocellulose membrane and immunoblotted was performed as described
874 previously in the section, *Immunoblotting*. Following ECL detection, VP40 cell lysate
875 ($VP40_{CL}$) expression was normalized to the respective GAPDH band density. The relative
876 budding index was calculated according to the ratio of $density_{VLP}/density_{C+VLP}$ (where
877 $density_{VLP}$ is the eVP40 VLP band density and $density_{C+VLP}$ is the eVP40 cell lysate + VLP
878 band density).

879 **Scanning electron microscopy**

880 HEK293 cells were transfected with FLAG-eVP40 and treated as described in the
881 previous section, *Cell Culture, Transfections & Pharmacological Treatments.* Cells were
882 scraped and collected through low-speed centrifugation at 48 hours post-transfection, and
883 stored in primary fixative (2% glutaraldehyde, 2% paraformaldehyde in 0.1 M cacodylate
884 buffer, pH 7.35) at 4°C until processing. During processing, samples were fixed to
885 coverslips and post-stained with 1% osmium tetroxide in 0.1 M cacodylate buffer.
886 Samples were extensively rinsed with water and dehydrated with a graded series of
887 ethanol followed by drying in a Tousimis 931 Supercritical Autosamdri® device. Prior to
888 imaging, samples were coated with 3 nm Iridium. A Field Emission Scanning Electron
889 Microscope Magellan 400 (FEI) (Hillsboro, OR) was used to collect images, with
890 assistance from Tatyana Orlova at the Notre Dame Integrated Imaging Facility.

891 **Transmission electron microscopy imaging**

892 VLPs were purified as previously described in *VLP Collections & Functional*
893 *Budding Assays.* Following ultracentrifugation, VLPs were resuspended in fixative (2.5%
894 glutaraldehyde in 0.1 M cacodylate buffer). Purified VLPs were applied onto glow
895 discharged carbon formvar grids and negatively stained using 4% uranyl acetate.
896 Samples were imaged with a FEI Tecnai T12 electron microscope equipped with a
897 tungsten source and operating at 80 kV. VLP length and diameter measurements were
898 quantified using ImageJ software. For diameter analysis, eight different diameters were
899 measured across random areas on each VLP, and the mean diameter was reported.
900

901 **Circular dichroism**

902 VLPs were produced in the presence of DMSO or fendiline and purified as
903 previously described in the *VLP collections* section. PB buffer was added to a 10-mm
904 path-length Spectrosil Far UV Quartz cuvette (Starna Cells CatID: 21-Q-10) and a
905 background spectra was collected and autosubtracted from VLP samples. VLP samples
906 were loaded into the 10-mm cuvette diluted in PB buffer to an approximate final protein
907 concentration of 30 µg/mL. Circular dichroism spectra of VLP samples were collected
908 between 200-280 nm at a 0.2 nm step size with 0.5 s time-per-point (with adaptive
909 sampling) using a Chirascan spectrometer (Applied Photophysics, Leatherhead, UK).
910 Absorbance spectra (Abs) and detector signal (hv) were collected simultaneously as
911 controls. After collecting the CD spectra, a microstir bar was added to the cuvette and
912 thermal melting was run from 20°C-93°C using a 0.5°C step ramping at 1.00°C/minute
913 with a tolerance of 0.20°C; simultaneously, spectra were collected at a single wavelength

914 of 220 nm with a time-per-point of 24 seconds. Absorbance spectra (Abs) and detector
915 signal (hv) were collected simultaneously as controls. At the end of thermal melting
916 measurement collection, temperature set-points were replaced with temperatures
917 measured by the sample handling unit. Data was converted from Chirascan filetype to
918 CSV and then extracted into GraphPad PRISM 7. Using the first derivative of the circular
919 dichroism spectral signal in respect to temperature, the maxima was taken as the melting
920 point of the sample. Melting temperatures of the three replicates were averaged for the
921 reported T_m.
922

923 **DiI entry assay**

924 VLPs produced from HEK293 cells expressing FLAG-eVP40 and eGP were
925 purified as previously described in the *Functional Budding Assays* section. DiI entry
926 assays were performed as described previously (Kuroda *et al*, 2015; Nanbo *et al*, 2018).
927 In brief, following ultra-centrifugation VLPs were resuspended in STE buffer and further
928 purified by filtering through a 0.22 µm filter. Protein content of VLP samples were
929 normalized to 0.1 µg/mL using STE buffer. VLPs were labeled with DiI for 1 hr at RT with
930 gentle agitation (final DiI = 0.06 µM). Following incubation, labeled VLP samples were
931 concentrated down to equal volumes, and brought up to volume in phenol-free MEM with
932 2% FBS and 4% BSA.

933 HEK293 cells were transfected with TIM-1 for 24 hours prior to incubation with DiI-
934 labeled VLPs and briefly rinsed with phenol-free MEM with 2% FBS and 4%BSA. DiI-
935 VLPs were added to TIM-1 expressing HEK293 cells, spinoculated for 45 min at 4°C, and
936 allowed to incubate for 1 hr at 37°C. Plates were then rinsed with PBS, fixed with 4%

937 paraformaldehyde in PBS, their nuclei stained with Hoechst 3342, and stored at 4°C until
938 imaging. During image acquisition, z-stacks were acquired of 10-15 frames (1 μm steps).
939

940 **Toxicity analysis**

941 HEK293 and Vero E6 cell toxicity following fendiline treatment was tested at the
942 indicated time points using the Cell Titer Glo Viability Assay (Promega, Madison WI)
943 according to the manufacturer's protocol. In brief, HEK293 cells were treated with the
944 indicated concentration of fendiline or control for 24 or 48 hours. Vero E6 cells were
945 treated for 24 hours, the drug was removed and the cells were replenished with Vero E6
946 culture media, to mirror the corresponding ebolavirus infections at BSL-4. Following the
947 one-hour mock infection, cells were washed with PBS and plates were divided into three
948 treatment groups (day 0, e.d., e.o.d.), and cells received either culture media or freshly
949 prepared fendiline or vehicle control and were then treated daily with freshly prepared
950 compound or left to incubate based on their designated treatment group. At 48, 72, and
951 96 hours following mock infection, and mirroring the post infection fixation time points,
952 CellTiter-Glo® reagent was added to each well in accordance with the manufacturer's
953 instructions. Both HEK293 and Vero E6 toxicity assays luminescence readings were
954 recorded using a SpectraMax® M5 (Molecular Devices®) plate reader.
955

956 **Mathematical model of *in vitro* experiments**

957 We implemented a system of ordinary differential equations (ODEs) to describe
958 the dynamics of host target cells, infected cells and free virus in different combinations
959 reflecting the *in vitro* experimental systems used here. These equations are similar to

those used to simulate Ebola virus dynamics in earlier work (Nguyen *et al*, 2015; Martyushev *et al*, 2016).

$$\frac{dT}{dt} = -\beta TV \quad (1)$$

$$\frac{dI}{dt} = \beta TV - \delta I \quad (2)$$

$$\frac{dV}{dt} = pI - cV \quad (3)$$

Where *T*, *I* and *V* represent numbers of susceptible target host cells, infected cells and free virions respectively and parameters are described in Table 2.

We modified appropriate parameters in equations 1-3 to represent the following experimental systems during calibration of the mathematical model:

- Viral budding assay (set β=0, T(0) = 0, I(0) = 2.625x10^6, V(0) = 0, vary δ, c, p)
- Viral entry assay (set p=0, T(0) = 6.3x10^5, I(0) = 0, V(0) = 6.3x10^3, vary β, δ, c)
- BSL-4 Cellular infection assay (BSL4) (T(0) = 5x10^4, I(0) = 0, V(0) = 5x10^4 (MOI 1) or V(0) = 5x10^3 (MOI 0.1) , vary β, δ, c, p)

Fendiline treatment effects are simulated using E_{max} dose response curves:

$$f_X = E_{max} \frac{C^H}{C_{50}^H + C^H}$$

Where *C*: concentration of fendiline, E_{max}: maximum effect of fendiline, *H*: hill constant for the dose response curve, and C_{50} concentration with 50% of E_{max} efficacy. E_{max}, C_{50} and *H* are fitted separately for fendiline effects on budding ($f_{budding}$) or entry (f_{entry}). Fendiline

982 efficacy (f_X) is defined as a fraction where f_X=0 implies no effect and f_X=1 implies 100%
983 inhibition of X (X = budding or entry). Fendiline effects are integrated into equations (1-3)
984 by multiplying β by (1-f_{entry}) and multiplying p by (1-$f_{budding}$). Fendiline concentrations are
985 assumed to be constant over the observation periods based on low *in vitro* degradation
986 rates of the drug. Daily treatment in the BSL-4 assays (e.d.) are simulated by removing
987 all free virus particles from the equations at each dosing time.

988 We calibrated the model in two stages. First, we calibrated to the budding and
989 entry assays. The uncoupling of budding and entry in this data allows us to define
990 biologically feasible ranges for the effects of fendiline on budding and entry separately.
991 Using these feasible ranges, we proceed to calibrate the full model to the BSL-4 data
992 (day-1/0 and e.d.). Therefore, we allow the budding and entry assays to inform the BSL-
993 4 simulations without imposing strict assumptions about the equivalency between the two
994 systems. In this way we progressively build complexity into the model accounting for
995 fendiline effects on viral budding, entry, and infection progression.

996 Calibrating to budding and entry assays we restrict the value of p to be larger than
997 1 and c to be between 0 and 5. These assumptions are in line with previous estimates,
998 and are necessary to qualitatively reproduce viral production observed, but not quantified,
999 in the budding assays. Parameters are estimated using Matlab's non-linear least squares
1000 optimization algorithm. Parameter bounds and final values are defined in Table 2.

1001

1002 **Statistical testing**

1003 All experiments were done in triplicate (unless otherwise noted and figure legends
1004 indicate the number of replicates). For analysis of eVLP diameter and length from TEM

experiments, as well as total PA levels between control and 5 μM fendiline treated cells, a two-tailed t-test was performed. For all experiments which contained >2 experimental groups, a one-way ANOVA with Dunnett's multiple comparisons was performed on raw data. Lastly, for N&B analysis, a two-way ANOVA with Dunnett's multiple comparisons was performed.

Data Availability

No data were deposited in a public database and any additional data from this paper can be requested from the authors.

Acknowledgements

These studies were supported by the NIH (AI081077) to R.V.S and the Indiana CTSI to E.P. and R.V.S. (UL1TR001108). M.L.H. was partially supported by a NIH T32 fellowship (T32 GM075762), E.A.D. was supported by NIH T32 fellowship (GM132024), and C.B.P. was supported by NIH T32 fellowship (AI148103). We are grateful for lipidomic analysis by Avanti Polar Lipids, Inc., and for research support by Dr. Nathan Dissinger. The authors acknowledge the use of the facilities of the Bindley Bioscience Center, a core facility of the NIH-funded Indiana Clinical and Translational Sciences institute and the use of the Purdue Life Science Electron Microscopy facility.

Author Contributions

Conceptualization: M.L.H. and R.V.S. Investigation: M.H., S.A., L.I.P., E.A.D., C.B.P., and K.E.H. Methodology: M.H., S.A., L.I.P., E.A.D., C.B.P., K.E.H., and L.I.P. designed the BSL-4 experiments. Formal analysis: M.H., S.A., L.I.P., E.A.D., C.B.P., L.I.P. and K.E.H.

performed and analyzed the BSL-4 experiments. E.P. designed and performed the mathematical modeling and analysis. Funding acquisition: M.L.H., E.A.D., C.B.P., E.P., and R.V.S. Project administration: R.V.S. Supervision: R.V.S. oversaw the in vitro and BSL-2 work, J.M.B. and J.D. oversaw the BSL-4 work, E.P. oversaw the mathematical modeling and analysis. Writing - original draft: M.L.H. and R.V.S. Writing – review and editing: all authors.

Conflict of Interest

The authors declare that they have no conflict of interest.

1038 **References**

1039 Adu-Gyamfi E, Digman MA, Gratton E, Stahelin R V (2012) Investigation of Ebola VP40
1040 assembly and oligomerization in live cells using number and brightness analysis.
1041 *Biophys J* 102: 2517–2525
1042 Adu-Gyamfi E, Soni SP, Xue Y, Digman MA, Gratton E, Stahelin RV (2013) The Ebola
1043 virus matrix protein penetrates into the plasma membrane: a key step in viral protein
1044 40 (VP40) oligomerization and viral egress. *J Biol Chem* 288: 5779-5789
1045 Adu-Gyamfi E, Johnson KA, Fraser ME, Scott JL, Soni SP, Jones KR, Digman MA,
1046 Gratton E, Tessier CR, Stahelin RV (2015) Host Cell Plasma Membrane
1047 Phosphatidylserine Regulates the Assembly and Budding of Ebola Virus. *J Virol* 89:
1048 9440-9453
1049 Amara A, Mercer J (2015) Viral apoptotic mimicry. *Nat Rev Microbiol* 13: 461–469
1050 Amiar S, Stahelin RV (2020) The Ebola virus matrix protein VP40 hijacks the host plasma
1051 membrane to form virus envelope. *J Lipid Res* 61: 971
1052 Amiar S, Husby ML, Wijesinghe KJ, Angel S, Bhattarai N, Gerstman BS, Chapagain PP,
1053 Li S, Stahelin RV (2021) Lipid-specific oligomerization of the Marburg virus protein
1054 VP40 is regulated by two distinct interfaces for virion assembly. *J Biol Chem* 296:
1055 100796
1056 Banadyga L, Dolan MA, Ebihara H (2016) Rodent-Adapted Filoviruses and the Molecular
1057 Basis of Pathogenesis. *J Mol Biol* 428: 3449–3466
1058 Bayer R, Mannhold R. (1987) Fendiline: a review of its basic pharmacological and clinical
1059 properties. *Pharmatherapeutica* 5: 103–136
1060 Bell RM, Ballas LM, Coleman RA (1981) Lipid topogenesis. *J Lipid Res* 22: 391–403
1061 Berjukow S, Doring F, Froschmayr M, Grabner M, Glossman H, Hering S (1996)
1062 Endogenous calcium channels in human embryonic kidney (HEK293) cells. *Br J*
1063 *Pharmacol* 118: 748-753
1064 Bobone S, Hilsch M, Storm J, Dunsing V, Herrmann A, Chiantia S (2017)
1065 Phosphatidylserine Lateral Organization Influences the Interaction of Influenza
1066 Virus Matrix Protein 1 with Lipid Membranes. *J Virol* 91: 1–15.
1067 Bolte S, Cordelières FP (2006) A guided tour into subcellular colocalization analysis in
1068 light microscopy. *J Microsc* 224: 213–232
1069 Bornholdt ZA, Noda T, Abelson DM, Halfmann P, Wood MR, Kawaoka Y, Sahpire EO
1070 (2013) Structural rearrangement of ebola virus vp40 begets multiple functions in
1071 the virus life cycle. *Cell* 154: 763–77
1072 Breman JG, Heymann DL, Lloyd G, McCormick JB, Miatudila M, Murphy FA, Muyembé-
1073 Tamfun JJ, Piot P, Ruppol JF, Sureau P, *et al* (2016) Discovery and Description of
1074 Ebola Zaire Virus in 1976 and Relevance to the West African Epidemic during 2013-
1075 2016. *J Infect Dis* 214: S93–S101
1076 Brunton B, Rogers K, Phillips EK, Brouillette RB, Bouls R, Butler NS, Maury W (2019)
1077 TIM-1 serves as a receptor for Ebola virus in vivo, enhancing viremia and
1078 pathogenesis. *PLoS Negl Trop Dis* 13: e0006983
1079 Carnec X, Meertens L, Dejarnac O, Perera-Lecoin M, Hafirassou ML, Kitaura J, Ramdasi
1080 R, Schwartz O, Amara A (2015) The Phosphatidylserine and
1081 Phosphatidylethanolamine Receptor CD300a Binds Dengue Virus and Enhances
1082 Infection. *J Virol* 90: 92–102
1083 Cheng JS, Wang JL, Lo YK, Chou KJ, Lee KC, Liu CP, Chang HT, Jan CR (2001) Effects

1084 of the antianginal drug fendiline on Ca2+ movement in hepatoma cells. *Hum Exp*
1085 *Toxicol* 20: 359-364
1086 Cho KJ, van der Hoeven D, Zhou Y, Maekawa M, Ma X, Chen W, Fairan GD, Hancock
1087 JF (2015) Inhibition of Acid Sphingomyelinase Depletes Cellular
1088 Phosphatidylserine and Mislocalizes K-Ras from the Plasma Membrane. *Mol Cell*
1089 *Biol* 36: 363–374
1090 Cho W, Stahelin RV (2005) Membrane-protein interactions in cell signaling and
1091 membrane trafficking. *Annu Rev Biophys Biomol Struct* 34: 119-151
1092 Darszon A, Vandenberg CA, Schönfeld M, Ellisman MH, Spitzer NC, Montal M (1980)
1093 Reassembly of protein-lipid complexes into large bilayer vesicles: perspectives for
1094 membrane reconstitution. *Proc Natl Acad Sci U S A* 77: 239–243
1095 Dejarnac O, Hafirassou ML, Chazal M, Versapuech M, Gaillard J, Perera-Lecoin M,
1096 Umana-Diaz C, Bonnet-Madin L, Carnec X, Tinevez JY *et al* (2018) TIM-1
1097 Ubiquitination Mediates Dengue Virus Entry. *Cell Rep* 23: 1779–1793
1098 Del Vecchio K, Frick CT, Gc JB, Oda S, Gerstman BS, Saphire EO, Chapagain PP,
1099 Stahelin RV (2018) A cationic, C-terminal patch and structural rearrangements in
1100 Ebola virus matrix VP40 protein control its interactions with phosphatidylserine. *J*
1101 *Biol Chem* 293: 3335–3349
1102 Digman MA, Dalal R, Horwitz AF, Gratton E (2008) Mapping the number of molecules
1103 and brightness in the laser scanning microscope. *Biophys J* 94: 2320–2332
1104 Dyall J, Nelson EA, DeWald LE, Guha R, Hart BJ, Zhou H, Postnikova E, Logue J, Vargas
1105 WM, Gross R, *et al* (2018) Identification of Combinations of Approved Drugs With
1106 Synergistic Activity Against Ebola Virus in Cell Cultures. *J Infect Dis* 218: S672–
1107 S678
1108 Fairn GD, Schieber NL, Ariotti N, Murphy S, Kuerschner L, Webb RI, Grinstein S, Parton
1109 RG (2011) High-resolution mapping reveals topologically distinct cellular pools of
1110 phosphatidylserine. *J Cell Biol* 194: 257–227
1111 Folch J, Lees M, Sloane Stanley GH (1957) A simple method for the isolation and
1112 purification of total lipides from animal tissues. *J Biol Chem* 226: 497–509
1113 Graul, AI, Pina, P, Tracy, M, Sorbera, L (2020) This year's new drugs and biologics. *Drugs*
1114 *Today* 56: 47-103
1115 Han Z, Madara JJ, Herbert A, Prugar LI, Ruthel G, Lu J, Liu Y, Liu W, Liu X, Wrobel JE
1116 *et al* (2015) Calcium regulation of hemorrhagic fever virus budding: Mechanistic
1117 implications for host-oriented therapeutic intervention. *PLoS Pathog* 11: e1005220
1118 Harty RN (2018) Hemorrhagic Fever Virus Budding Studies. In: *Hemorrhagic Fever*
1119 *Viruses: Methods and Protocols*, Salvato MS (ed) pp. 209–215. Springer New York,
1120 New York, USA.
1121 Hirama T, Das R, Yang Y, Ferguson C, Won A, Yip CM, Kay JG, Grinstein S, Parton RG,
1122 Fairn GD (2017) Phosphatidylserine dictates the assembly and dynamics of
1123 caveolae in the plasma membrane. *J Biol Chem* 292: 14292–14307
1124 Hoenen T, Biedenkopf N, Zielecki F, Jung S, Groseth A, Feldmann H, Becker S (2010)
1125 Oligomerization of Ebola virus VP40 is essential for particle morphogenesis and
1126 regulation of viral transcription. *J Virol* 84: 7053–7063
1127 Huang CC, Huang CJ, Cheng JS, Liu SI, Chen IS, Tsai JY, Chou CT, Tseng PL, Jan CR
1128 (2009) Fendiline-evoked [Ca2+]i rises and non-Ca2+-triggered cell death in human
1129 oral cancer cells. *Hum Exp Toxicol* 28: 41-48

1130 Jan CR, Tseng CJ, Chen WC (2000) Fendiline increases [Ca2+]I in Madin Darby canine
1131 kidney (MDCK) cells by releasing internal Ca2+ followed by capacitative Ca2+
1132 entry. *Life Sci* 66: 1053-1062
1133 Jan CR, Lee KC, Chou KJ, Cheng JS, Wang JL, Lo YK, Chang HT, Tang KY, Yu CC,
1134 Huang JK (2001) Fendiline, an anti-anginal drug, increases intracellular Ca2+ in
1135 PC3 human prostate cancer cells. *Cancer Chemother Pharmacol* 48: 37-41
1136 Jasenosky LD, Cadena C, Mire CE, Borisevich V, Haridas V, Ranjbar S, Nambu A, Bavari
1137 S, Soloveva V, Sadukhan S *et al* (2019) The FDA-Approved Oral Drug
1138 Nitazoxanide Amplifies Host Antiviral Responses and Inhibits Ebola Virus. *iScience*
1139 19: 1279–1290
1140 Jasenosky LD, Neumann G, Lukashevich I, Kawaoka Y (2001) Ebola virus VP40-induced
1141 particle formation and association with the lipid bilayer. *J Virol* 75: 5205–5214
1142 Jasenosky LD, Kawaoka Y (2004) Filovirus budding. Virus Res. 106: 181–188.
1143 Jemielity S, Wang JJ, Chan YK, Ahmed AA, Li W, Monahan S, Bu X, Farzan M, Freeman
1144 GJ, Umetsu DT *et al* (2013) TIM-family Proteins Promote Infection of Multiple
1145 Enveloped Viruses through Virion-associated Phosphatidylserine. *PLoS Pathog* 9:
1146 e1003232.
1147 Johansen LM, Brannan JM, Delos SE, Shoemaker CJ, Stossel A, Lear C, Hoffstrom BG,
1148 Evans Dewald L Schornberg KL, Scully C *et al* (2013) FDA-approved selective
1149 estrogen receptor modulators inhibit Ebola virus infection. Sci Transl Med 5:
1150 190ra79
1151 Johansen LM, DeWald LE, Shoemaker CJ, Hoffstrom BG, Lear-Rooney CM, Stossel A,
1152 Nelson E, Delos SE, Simmons JA, Greiner JM *et al* (2015) A screen of approved
1153 drugs and molecular probes identifies therapeutics with anti-Ebola virus activity. *Sci*
1154 *Transl Med* 7: 290ra89
1155 Johnson KA, Budicini MR, Urata S, Gerstman BS, Chapagain PP, Li S, Stahelin RV
1156 (2018) PI(4,5)P2 Binding Sites in the Ebola Virus Matrix Protein Modulate Assembly
1157 and Budding. *bioRxiv* doi:10.1101/341248
1158 Johnson, KA, Bhattarai N, Budicini MR, LaBonia CM, Baker SCB, Gerstman BS,
1159 Chapagain PP, Stahelin RV (2021) Cysteine mutations in the Ebolavirus matrix
1160 protein VP40 promote Phosphatidylserine bniding by increasing the flexibility of a
1161 lipid-binding loop. *Viruses* 13: 1375
1162 Johnson KA, Taghon GJF, Scott JL, Stahelin R V (2016) The Ebola Virus matrix protein,
1163 VP40, requires phosphatidylinositol 4,5-bisphosphate (PI(4,5)P2) for extensive
1164 oligomerization at the plasma membrane and viral egress. *Sci Rep* 6: 19125
1165 Kay JG, Koivusalo M, Ma X, Wohland T, Grinstein S (2012) Phosphatidylserine dynamics
1166 in cellular membranes. *Mol Biol Cell* 23: 2198–2212
1167 Kerr D, Tietjen GT, Gong Z, Tajkhorshid E, Adams EJ, Lee KYC (2018) Sensitivity of
1168 peripheral membrane proteins to the membrane context: A case study of
1169 phosphatidylserine and the TIM proteins. *Biochim Biophys acta Biomembr* 1860:
1170 2126–2133
1171 Kondratowicz AS, Lennemann NJ, Sinn PL, Davey RA, Hunt CL, Moller-Tank S,
1172 Meyerholz DK, Rennert P, Mullins PF, Brindley M, *et al* (2011) T-cell
1173 immunoglobulin and mucin domain 1 (TIM-1) is a receptor for Zaire Ebolavirus and
1174 Lake Victoria Marburgvirus. *Proc Natl Acad Sci U S A* 108: 8426–8431
1175 Kuroda M, Fujikura D, Nanbo A, Marzi A, Noyori O, Kajihara M, *et al* (2011) Interaction

1176 Between TIM-1 and NPC1 Is Important for Cellular Entry of Ebola Virus. *J Virol* 89:
1177 6481–6493
1178 Kurovetz WR, Brunner F, Beubler E, Weyhenmeyer R, Lohaus R, Grob M, Mayer D
1179 (1982) Single dose pharmacokinetics of fendiline in humans. *Eur J Drug Metab*
1180 *Pharmaco*kinet 7: 105-110
1181 Licata JM, Simpson-Holley M, Wright NT, Han Z, Paragas J, Harty RN (2003) Overlapping
1182 Motifs (PTAP and PPEY) within the Ebola Virus VP40 Protein Function
1183 Independently as Late Budding Domains: Involvement of Host Proteins TSG101
1184 and VPS-4. *J Virol* 77: 1812–1819
1185 Liu L (2014) Fields Virology, 6th Edition. *Clin Infect Dis* 59: 613–613
1186 Llorente A, Skotland T, Sylvänne T, Kauhanen D, Rog T, Orlowski A, Vattulainen I, Ekroos
1187 K, Sandvig K (2013) Biochim Biophys Acta 1831: 1302-1309
1188 Madara JJ, Han Z, Ruthel G, Freedman BD, Harty RN (2015) The multifunctional Ebola
1189 virus VP40 matrix protein is a promising therapeutic target. *Future Virol* 10: 537-
1190 546.
1191 Maekawa M, Fairn GD (2015) Complementary probes reveal that phosphatidylserine is
1192 required for the proper transbilayer distribution of cholesterol. *J Cell Sci* 128: 1422-
1193 1433.
1194 Maekawa M, Lee M, Wei K, Ridgway ND, Fairn GD (2016) Staurosporines decrease
1195 ORMDL proteins and enhance sphingomyelin synthesis resulting in depletion of
1196 plasmalemmal phosphatidylserine. *Sci Rep* 6: 35762
1197 Martyushev A, Nakaoka S, Sato K, Noda T, Iwami S (2016) Modelling Ebola virus
1198 dynamics: Implications for therapy. *Antiviral Res* 135: 62–73.
1199 Menke M, Gerke V, Steinem C (2005) Phosphatidylserine membrane domain clustering
1200 induced by annexin A2/S100A10 heterotetramer. *Biochemistry* 44: 15296–15303
1201 Miller ME, Adhikary S, Kolokoltsov AA, Davey RA (2012) Ebolavirus Requires Acid
1202 Sphingomyelinase Activity and Plasma Membrane Sphingomyelin for Infection. *J*
1203 *Virol* 86: 7473–7483
1204 Moe JB, Lambert RD, Lupton HW (1981) Plaque assay for Ebola virus. *J Clin Microbiol*
1205 13: 791–793.
1206 Moller-Tank S, Kondratowicz AS, Davey RA, Rennert PD, Maury W (2013) Role of the
1207 phosphatidylserine receptor TIM-1 in enveloped-virus entry. *J Virol* 87: 8327–8341.
1208 Moller-Tank S, Maury W (2014) Phosphatidylserine receptors: Enhancers of enveloped
1209 virus entry and infection. *Virology* 468-470: 565–580.
1210 Mühlberger E (2007) Filovirus replication and transcription. *Future Virol* 2: 205–215.
1211 Mullard, A (2020) FDA approves antibody cocktail for Ebola virus. *Nat Rev Drug Discov*
1212 19: 827
1213 Nanbo A, Imai M, Watanabe S, Noda T, Takahashi K, Neumann G, Halfmann P, Kawoaka
1214 Y (2010) Ebolavirus is internalized into host cells via macropinocytosis in a viral
1215 glycoprotein-dependent manner. *PLoS Pathog* 6: e1001121
1216 Nanbo A, Kawaoka Y (2019) Molecular Mechanism of Externalization of
1217 Phosphatidylserine on the Surface of Ebola Virus Particles. *DNA Cell Biol* 38: 115–
1218 120
1219 Nanbo A, Maruyama J, Imai M, Ujie M, Fujioka Y, Nishide S, Takada A, Ohba Y, Kawoaka
1220 Y (2018) Ebola virus requires a host scramblase for externalization of
1221 phosphatidylserine on the surface of viral particles. *PLoS Pathog* 14: e1006848

1222 Nelson EA, Barnes AB, Wiehle RD, Fontenot GK, Hoenen T, White JM (2016)
1223 Clomiphene and Its Isomers Block Ebola Virus Particle Entry and Infection with
1224 Similar Potency: Potential Therapeutic Implications. *Viruses* 8: 206.
1225 Nguyen VK, Binder SC, Boianelli A, Meyer-Hermann M, Hernandez-Vargas EA (2015)
1226 Ebola virus infection modeling and identifiability problems. *Front Microbiol.* 6: 257
1227 Noda T, Sagara H, Suzuki E, Takada A, Kida H, Kawaoka Y (2002) Ebola Virus VP40
1228 Drives the Formation of Virus-Like Filamentous Particles Along with GP. *J Virol* 76:
1229 4855–4865
1230 Oda S, Noda T, Wijesinghe KJ, Halfmann P, Bornholdt ZA, Abelson DM, Armbrust T,
1231 Kawoaka Y, Stahelin RV, Saphire EO (2015) Crystal Structure of Marburg Virus
1232 VP40 Reveals a Broad, Basic Patch for Matrix Assembly and a Requirement of the
1233 N-Terminal Domain for Immunosuppression. *J Virol* 90: 1839–1848
1234 Panchal RG, Ruthel G, Kenny TA, Kallstrom GH, Lane D, Badie SS, Li L, Bavari S, Aman
1235 MJ. (2003) In vivo oligomerization and raft localization of Ebola virus protein VP40
1236 during vesicular budding. *Proc Natl Acad Sci U S A* 100: 15936–15941
1237 Reeves JP, Dowben RM (1969) Formation and properties of thin-walled phospholipid
1238 vesicles. *J Cell Physiol* 73: 49–60
1239 Reimão JQ, Mesquita JT, Ferreira DD, Tempone AG (2016) Investigation of calcium
1240 channel blockers as antiprotozoal agents and their interference in the metabolism
1241 of Leishmania (L.) infantum. *Evid Based Complement Alternat Med* 2016: 1523691
1242 Ruigrok RW, Schoehn G, Dessen A, Forest E, Volchkov V, Dolnik O, Klenk HD,
1243 Weissenhorn W (2000) Structural characterization and membrane binding
1244 properties of the matrix protein VP40 of Ebola virus. *J Mol Biol* 300: 103–112
1245 Scianimanico S, Schoehn G, Timmins J, Ruigrok RH, Klenk HD, Weissenhorn W (2000)
1246 Membrane association induces a conformational change in the Ebola virus matrix
1247 protein. *EMBO J* 19: 6732–6741
1248 Skotland T, Sandvig K (2019) The role of PS 18:0/18:1 in membrane function. *Nat*
1249 *Commun* 10: 2752
1250 Soni SP, Stahelin RV (2014) The Ebola virus matrix protein VP40 selectively induces
1251 vesiculation from phosphatidylserine-enriched membranes. *J Biol Chem* 289:
1252 33590–33597
1253 Stahelin RV (2014) Membrane binding and bending in Ebola VP40 assembly and egress.
1254 *Front Microbiol* 5: 300
1255 Stahelin RV, Scott JL, Frick CT (2014) Cellular and molecular interactions of
1256 phosphoinositides and peripheral proteins. *Chem Phys Lipids* 182: 3–18.
1257 Tsai WH (1985) Moment-preserving thresolding: A new approach. *Comput Vision, Graph*
1258 *Image Process* 29: 377–393
1259 van der Hoeven D, Cho K, Ma X, Chigurupati S, Parton RG, Hancock JF (2013) Fendiline
1260 inhibits K-Ras plasma membrane localization and blocks K-Ras signal
1261 transmission. *Mol Cell Biol* 33: 237–251
1262 van der Hoeven D, Cho K, Zhou Y, Ma X, Chen W, Naji A, Montufar-Solis D, Zuo Y, Kovar
1263 SE, Levental I et al (2018) Sphingomyelin Metabolism Is a Regulator of K-Ras
1264 Function. *Mol Cell Biol* 38: e00373-17
1265 Van Meer G, Voelker DR, Feigenson GW (2008) Membrane lipids: Where they are and
1266 how they behave. *Nat Rev Mol Cell Biol* 9: 112–124.
1267 Wan W, Clarke M, Norris MJ, Kolesnikova L, Koehler A, Bornholdt ZA, Becker S, Saphire

1268 EO, Briggs JA (2020) Ebola and Marburg virus matrix layers are locally ordered
1269 assemblies of VP40 dimers. *Elife* 9: e592225
1270 Wang YE, Park A, Lake M, Pentecost M, Torres B, Yun TE, Wolf MC, Holbrook MR,
1271 Freiberg AN, Lee B (2010) Ubiquitin-regulated nuclear-cytoplasmic trafficking of the
1272 Nipah virus matrix protein is important for viral budding. *PLoS Pathog* 6: e1001186
1273 Wang J, Qiao L, Hou Z, Luo G (2017) TIM-1 Promotes Hepatitis C Virus Cell Attachment
1274 and Infection. *J Virol* 91: e01583-16
1275 Wang P, van der Hoeven D, Ye N, Chen H, Liu Z, Ma X, Montufar-Solis D, Rehl KM,
1276 Cho KJ, Thapa S *et al* (2021) Scaffold repurposing of fendiline: Identification of
1277 potent KRAS plasma membrane localization inhibitors. *Eur J Med Chem* 217:
1278 113381.
1279 Watt A, Moukambi F, Banadyga L, Groseth A, Callison J, Herwig A, Ebihara H, Feldmann
1280 H, Hoenen T (2014) A Novel Life Cycle Modeling System for Ebola Virus Shows a
1281 Genome Length-Dependent Role of VP24 in Virus Infectivity. *J Virol* 88: 10511–
1282 10524
1283 Wen Y, Vogt VM, Feigenson GW (2018) Multivalent Cation-Bridged PI(4,5)P2 Clusters
1284 Form at Very Low Concentrations. *Biophys J* 114: 2630–2639
1285 Weyhenmeyer R, Fenzl E, Apecechea M, Rehm KD, Dyde CJ, Johnson KJ, Friedel R
1286 (1987) Tolerance and pharmacokinetics of oral fendiline. *Arzneimittelforschung* 37:
1287 58-62
1288 Wijesinghe KJ, Stahelin V (2015) Investigation of the Lipid Binding Properties of the
1289 Marburg Virus. *J Virol* 90: 3074–3085
1290 Xiao X, Wang C, Chang D, Wang Y, Dong X, Jiao T, Zhao Z, Ren L, Dela Cruz CS,
1291 Sharma L *et al* (2020) Identification of potent and safe antiviral therapeutic
1292 candidates against SARS-CoV-2. *Front Immunol* 11: 586572
1293 Yamashita Y, Oka M, Tanaka T, Yamazaki M (2002) A new method for the preparation
1294 of giant liposomes in high salt concentrations and growth of protein microcrystals
1295 in them. *Biochim Biophys Acta* 1561: 129–134
1296 Yeung T, Gilbert GE, Shi J, Silvius J, Kapus A, Grinstein S (2008) Membrane
1297 phosphatidylserine regulates surface charge and protein localization. *Science* 319:
1298 210–213
1299 Younan P, Iampietro M, Santos RI, Ramanathan P, Popov VL, Bukreyev A (2018)
1300 Disruption of Phosphatidylserine Synthesis or Trafficking Reduces Infectivity of
1301 Ebola Virus. *J Infect Dis* 218: S475–S485
1302 Zhao H, Hakala M, Lappalainen P (2010) ADF/cofilin binds phosphoinositides in a
1303 multivalent manner to act as a PIP(2)-density sensor. *Biophys J* 98: 2327–2336
1304
1305

Figure Legends

Figure 1

Clustering of PS by eVP40 *in vitro* and in HEK 293 cells. A Representative 3D reconstructed confocal images of immobilized GUVs (DPPC:Cholesterol:DPPS:PI(4,5)P_2:TopFluor® TMR-PS(red)). Left panel: GUVs incubated without eVP40-Alexa488. Right three panels: GUVs incubated with 1.25 μM eVP40-Alexa488 (green). **B** Index of correlation (Mander's coefficient) between TopFluor® TMR-PS and eVP40-Alexa488 of different GUVs compositions incubated with 1.25 μM eVP40-Alexa488. Values are reported as mean ± s.d. A one-way ANOVA with multiple comparisons was performed (n = 3); ****$p<0.0001$. **C** % TopFluor® TMR-PS quenching by eVP40 using GUVs (DPPC:Cholesterol:TopFluor®TMR-PS + increasing mol% of PS), 2.5% PI(4,5)P_2 was added to GUVs with 60% PS. Fluorescence spectra were recorded (Ex: 547 nm; Em: 550-600 nm); n=2. **D** Representative confocal images of HEK293 cells expressing various GFP-fused proteins (green) and supplemented with TopFluor® TMR-PS (red); scale bar= 10 μm. Yellow arrows indicate high intensity PS fluorescence regions **E** %PM with PS clusters = area of high intensity fluorescent PS clusters over total plasma membrane area from images in panel D. Black bars are control proteins and blue bars are eVP40 proteins. Values are reported as mean ± s.d.; N>18, n=3; A one-way ANOVA was performed with multiple comparisons compared to the control GFP %PS clustering (***$p=0.0007$, **$p=0.004$). DPPC: dipalmitoyl-phosphatidylcholine; DPPS: dipalmitoyl-phosphatidylserine; GUVs: giant unilamellar vesicles; PS: phosphatidylserine; PM: plasma membrane.

Figure 2

Effect of PS concentration on eVP40 binding affinity to and oligomerization on membranes. A-C SPR demonstrates that eVP40 affinity to LUVs increases in relation to PS concentration. **A** Representative normalized sensorgram of His_6-eVP40 binding to LUVs containing 1% PS indicating an apparent affinity of 2.5 μM. **B** Representative normalized sensorgram of His_6-eVP40 binding to LUVs containing 11% PS indicating an apparent affinity of 0.65 μM. **C** Representative normalized sensorgram of His_6-eVP40 binding to LUVs containing 22% PS indicating an apparent affinity of 0.18 μM. **D-E** PS concentration in LUVs enhances the ability of His_6-eVP40 to oligomerize on membranes. **D** Representative western blot of chemical crosslinking performed on His_6-WT-eVP40 following incubation with LUVs of varying PS content (detected by Mouse α-His antibody & HRP-Sheep α-Mouse). **E** Oligomerization capacity was determined from the western blot band density ratio of oligomers/(monomer + dimer) from chemical crosslinking experiments. A one-way ANOVA was performed with multiple comparisons compared to the control 0% PS LUVs control (30% PS *p= 0.021; 60% PS *p=0.017). n=3**.** Values are reported as mean ± s.d.; SPR: surface plasmon resonance; LUVs: large unilamellar vesicles; PS: phosphatidylserine; HRP: horseradish peroxidase.

Figure 3

PS concentration, localization, and dynamics in fendiline treated HEK293 cells. A Lipidomic analysis (LC/MS/MS) of total lipids extracted from HEK293 cells treated with the indicated concentration of fendiline (48 hours) demonstrated a significant reduction of total cellular PS levels. Values are normalized to DMSO control and are reported as mean

± s.d.; n=3; A one-way ANOVA was performed with multiple comparisons to the control DMSO (*p=0.0120, ***p=0.0003). **B-C** Analysis of PS plasma membrane localization in response to fendiline treatment in HEK293 cells. **B** Representative confocal images from live cell imaging of HEK293 cells expressing GFP-LactC2 and treated with fendiline for 48 hours; scale bars= 10 µm. **C** Effect of fendiline on PS plasma membrane localization was calculated by the ratio of GFP fluorescence at the plasma membrane intensity/intracellular intensity. Values are normalized to DMSO control and are reported as mean ± s.d.; N>15, n=3; A one-way ANOVA was performed with multiple comparisons compared to the DMSO control (**p=0.0031) **D-E** Analysis of PS clustering in HEK293 cells in response to fendiline treatment through N&B analysis. **D** *Left panel:* Representative images from time-lapse (30 frames) imaging of HEK293 expressing GFP-LactC2 and treated with fendiline for 48 hours; scale bar= 5 µm. *Middle panel:* Brightness and Intensity plots for each representative image. *Right panel:* Selection map correlating each pixel in the representative image to an oligomerization state (b value) (red: monomer-5mer, green: 5mer-10mer, blue: >10mer). **E** Average % pixels quantification from panel (d)= Percentage of GFP-LactC2 with brightness values corresponding to monomer-5mer (~1.-1.5), 5mer-10mer (~1.5-1.9) and >10mer (>1.9) over the total pixels within each image. Values are reported as mean ± s.d.; N≥9, n=3; A two-way ANOVA was performed with Dunnett's multiple comparisons comparted to the control DMSO % average pixels (****p<0.0001, **p=0.0043).GFP-LactC2: phosphatidylserine sensor; N&B: Number & Brightness analysis; PM: plasma membrane; PS: phosphatidylserine.

<u>Figure 4</u>

Evaluation of fendiline efficacy in the inhibition of authentic EBOV spread. A-D Effect of fendiline on EBOV infection. **A** Representative confocal images of Vero E6 cells infected with EBOV (Kikwit) at the indicated MOI and treated with the indicated concentration of fendiline. Cells were pretreated 24 hours prior to infection with the indicated concentration of fendiline. Post infection, cells were treated 1 hour later (d -1/0), treated every day (e.d), or treated every other day (e.o.d) and fixed at either 48 hours, 72 hours or 96 hours post infection. (green=EBOV; blue= nuclei). White numbering in top right corner indicates %infection. **B-D** Quantification of % inhibition of EBOV by fendiline. **B** 48 hours (MOI 1.0) **C** 72 hours (MOI 0.1) **D** 96 hours (MOI 0.1). Values are reported as mean ± s.d. A one-way ANOVA was performed with multiple comparisons was performed. n=3. EBOV: Ebola virus; MOI: multiplicity of infection; d. -1/0: treatment 1 hour after infection; e.d.: treatment every day; e.o.d.: treatment every other day.

Figure 5

Analysis of eVP40 and mVP40 cellular localization and oligomerization following fendiline treatment. A-C Effect of fendiline on eVP40 and mVP40 PM localization in HEK293 cells after 48 hours of treatment. **A** Representative confocal images from live cell imaging experiments of HEK293 cells expressing EGFP-WT-eVP40 (top panel) and EGFP-WT-mVP40 (bottom panel) after 48 hours of fendiline treatment. scale bars= 10 µm. Effect of fendiline on eVP40 **(B)** and mVP40 **(C)** PM localization was quantified by the ratio of EGFP fluorescence intensity at the PM / total EGFP fluorescence intensity (and normalized to DMSO control). N>15, n=3. Values are reported as mean ± s.d. A one-way ANOVA with multiple comparisons was performed compared to the DMSO control.

D-E Analysis of eVP40 oligomerization in HEK293 cells in response to 48 hour fendiline treatment using N&B analysis. **D** *Left panel:* Representative images from time-lapse (30 frames) of HEK293 expressing EGFP-WT-eVP40 and treated with fendiline for 48 hours. scale bar = 5 μm. *Middle panel:* Brightness and Intensity plots for each representative image. *Right panel:* Selection map correlating each pixel in the representative image to an oligomerization state (b value) (red: monomer-hexamer, green: hexamer-12mer, blue: 12mer-24mer, pink: >24mer). **E** Average % pixel quantification from panel (d)= % of GFP-WT-eVP40 with brightness values corresponding to monomer-hexamer (~1.-1.6), hexamer-12mer (~1.6-2.0), 12mer-24mer (2.0-3.2) and >24mer (>3.2) over the total pixels within each image. Values are reported as mean ± s.d.; N≥9, n=3; A two-way ANOVA was performed with Dunnett's multiple comparisons compared to the control DMSO % average pixels (**p=0.0035). PM: plasma membrane; N&B: Number & Brightness analysis.

Figure 6

VLP production and morphology in HEK293 cells in the presence of fendiline. A-D Functional budding assays assessed at 24 hours (A-B) and 48 hours (C-D) post treatment. **A** Representative western blot of budding assays performed at 24 hours. VLP samples (top panel) and cell lysate samples (bottom panel) collected from HEK293 cells and immunoblotted for eVP40 expression; GAPDH served as a loading control. eVP40 detected by (Rabbit α-eVP40 and HRP-Goat α-Rabbit); GAPDH detected by mouse α-GAPDH and HRP-Sheep α-Mouse) **B** Quantification of relative budding index at 24 hours post fendiline treatment. Relative budding index was determined by the western blot band

density of eVP40 in the VLP fraction/(total eVP40 cell lysate + eVP40 VLP band density) and was normalized to the DMSO control. Cell lysate eVP40 band density was normalized to GAPDH band density prior to use in budding index quantification. n=3. Values are reported as mean ± s.d. A one-way ANOVA was performed with multiple comparisons compared to the DMSO control. **C** Representative western blot of budding assays performed at 48 hours. VLP samples (top panel) and cell lysate samples (bottom panel) collected from HEK293 cells and immunoblotted for eVP40 expression; GAPDH served as a loading control. eVP40 detected by (Rabbit α-eVP40 and HRP-Goat α-Rabbit); GAPDH detected by (Mouse α-GAPDH and HRP-Sheep α-Mouse) **D** Quantification of relative budding index at 48 hours post fendiline treatment. Relative budding index was determined by the western blot band density of eVP40 in the VLP fraction/(total eVP40 cell lysate + eVP40 VLP band density) and was normalized to the DMSO control. Cell lysate eVP40 band density was normalized to GAPDH band density prior to use in budding index quantification. n=3. Values are reported as mean ± s.d. A one-way ANOVA was performed with multiple comparisons compared to the DMSO control. (*p=0.0260) **E-F** SEM micrographs of HEK93 cells. **E** Representative micrographs of mock transfected HEK293 cells harvested after 48 hours of no treatment or DMSO treatment. **F** Representative micrographs of HEK293 cells expressing FLAG-eVP40 and harvested after 48 hours of no treatment, DMSO treatment, or the indicated concentration of fendiline. VLPs: virus like particles; SEM: scanning electron microscopy; GAPDH: glyceraldehyde 3-phosphate dehydrogenase; HRP: horseradish peroxidase.

Figure 7

Effect of fendiline on eVLP morphology and TIM-1 dependent eVLP entry. **A-C** TEM analysis of eVLP morphology. **A** Representative transmission electron micrographs of eVLPs purified from HEK293 cells expressing FLAG-eVP40 and eGP following 48 hours of DMSO (left panel) or 5 μM fendiline treatment (right panel). **B** Quantification of eVLP length (μm) of DMSO-derived eVLPs (black) and fendiline-derived eVLPs (blue). N>50, n=3. Values are reported as mean ± s.d. A two-tailed t-test was performed (**p=0.0139). **C** Quantification of eVLP diameter (nm) of DMSO-derived eVLPs (black) and fendiline-derived eVLPs (blue). N>50, n=3. Values are reported as mean ± s.d. A two-tailed t-test was performed (*p=0.0430). **D-E** Fluorescence based DiI TIM-1 dependent entry assay. **D** Representative confocal images from the DiI-entry assay comparing entry of eVLPs produced from DMSO (top panel) and fendiline-treated HEK293 cells (bottom panel) into target cells (HEK293 cells transiently expressing increasing amounts of TIM-1; 0.0 μg, 0.5 μg, 1.0 μg). A stack of 10 frames was acquired for each image. DiI (initially red) was recolored to yellow for easier observation in print; blue (Hoechst 3342 stain); scale bar = 10 μm. **E** Quantification of eVLP entry was performed by calculating the total number of DiI punctate / the total number of DiI-positive cells. Three images from each z-stack was quantified. N=9, n=3. Values are reported as mean ± s.d. A one-way ANOVA was performed with multiple comparisons against the 0.0 μg TIM-1 condition for both DMSO- and fendiline derived eVLPs.(****p<0.0001; **p=0.0093). eVLP: entry-competent viral like particles; TEM: transmission electron microscopy; TIM-1: t-cell immunoglobulin receptor-1; eVLPs: entry-competent VLPs; eGP: Ebola glycoprotein; DiI: 1,1'-Dioctadecyl-3,3,3',3'-Tetramethylindocarbocyanine Perchlorate.

Figure 8

Calibrated mathematical model reproduces key observations in multiple experimental datasets. Percentage infected cells is shown for various fendiline concentrations given prior to infection (d-1/0, **A-C**) or daily (e.d., **D-F**). (**A,D**) MOI 1; (**B,C,E,F**) MOI 0.1. (**G-H**) Model predicted cell and viral dynamics for MOI 0.1. (**i**) Model predicted dose response curves for fendiline effects on viral budding and entry in the BSL4 experiments.

Expanded View Figure Legends

Expanded View 1 (EV1)

Fluorescence profiles of PS and WT-eVP40 through confocal microscopy and plot profile analysis of fluorescently labeled GUVs and Alexa488-eVP40. **A** Representative confocal images of fluorescently labeled (TopFluor® TMR-PS) GUVs with varying lipid compositions (red) following incubation with eVP40-Alexa88 (green). Colocalization between eVP40 and PS within GUVs was indicated by plot profile analyses of fluorescence signals between TopFluor® TMR-PS (red dotted line) and eVP40-Alexa488 (green solid line) performed at indicated open yellow lines in **a** and shown in **B-D**. **B** Plot profile analysis of eVP40-Alexa488 and control GUVs (DPPC:Cholesterol:0.2mol% TopFluor® TMR-PS), **C** Plot profile analysis of eVP40-Alexa488 and PS GUVs (DPPC:Cholesterol:0.2mol% TopFluor® TMR-PS:DPPS). * indicates overlap in fluorescence signals. **D** Plot profile analysis of eVP40-Alexa488 and PS+PI(4,5)P_2 GUVs (DPPC:Cholesterol:0.2mol% TopFluor® TMR-PS:DPPS:PI(4,5)P_2). **E** Plot of WT eVP40 Alexa-488 membrane fluorescence/total fluorescence for lipid

compositions shown in a-d, n = 3, ****p<0.0001. PS: phosphatidylserine; DPPC: dipalmitoyl-phosphatidylcholine; DPPS: dipalmitoyl-phosphatidylserine.

Expanded View 2 (EV2)

Fluorescence profiles of PS and GFP-WT-eVP40 in HEK 293 cells through confocal microscopy. A Representative confocal images from live cell imaging of HEK293 expressing various GFP-fused proteins (GFP; green) following supplementation with TopFluor® TMR-PS (red). Solid white lines indicate where plot profile analysis was performed; scale bar= 10 µm. **B-C** Validation of ability to detect exogenously added fluorescently labelled PS within the inner leaflet of the plasma membrane of cells **B** Plot profile analysis of HEK293 cells expressing cytosolic GFP. **C** Plot profile analysis of HEK293 cells expressing the PS sensor GFP-LactC2 **D-E** Investigation of functionally distinct eVP40 proteins ability to bind to fluorescently labelled PS within the inner leaflet of the plasma membrane in living cells. **D** Plot profile analysis of HEK293 cells expressing GFP-WT-eVP40. **E** Plot profile analysis of HEK293 cells expressing GFP-K224A-eVP40 (PS-binding residue mutant). **F** Plot profile analysis of HEK293 cells expressing GFP-WE/A-eVP40 (oligomerization deficient mutant). TopFluor TMR-PS fluorescence signal intensity (red dotted line) and GFP fluorescence signal intensity (green solid line).

Expanded View 3 (EV3)

Validation of in vitro and cellular PS clustering experiments. **A** GUVs of varying compositions were imaged prior to and following the addition of 1.25 µM eVP40-Alexa. eVP40-Alexa 488 enrichment ratios at the membrane of the GUVs were calculated by the

ratio the Alexa488 fluorescence intensity at the GUV membrane / Alexa488 total fluorescence. Values are reported as mean ± s.d.; of n=3. A two-way ANOVA with multiple comparisons was performed. *p<0.0001. **B** Representative images of the step-wise image analysis workflow of quantifying PS clustering in living HEK293 cells expressing GFP-fused proteins using a custom ImageJ macro. scale bar= 10 µm. **C** Representative images from live cell imaging experiments of HEK293 cells expressing control GFP-fused proteins specific for the plasma membrane (GPI), and specific lipids, PS (LactC2) and PI(4,5)P_2 (PLCδ-PH). scale bar = 10 µm.

Expanded View 4 (EV4)

Profile of fendiline toxicity and efficacy in BSL-2 models. A CellTiter-Glo® viability results of HEK293 cells. HEK293 cells were treated with fendiline for 24 hours (black line) and 48 hours (blue line) and viability was assessed as a % viability of control (n = 3). **B** PS saturation analysis from lipidomic analysis (LC/MS/MS) of total lipids extracted from HEK293 cells treated with the indicated concentration of fendiline (48 hours). Values are normalized to DMSO control and are reported as mean ± s.d.; n=3; A one-way ANOVA was performed with multiple comparisons compared to the control DMSO. **C** PA level analysis from lipidomic analysis (LC/MS/MS) of total lipids extracted from HEK293 cells treated with 5 µM fendiline (48 hours). Values are normalized to DMSO control and are reported as mean ± s.d.; n=3; A two-tailed t-test was performed. **D-E** Analysis of PS plasma membrane localization in response to 24 hour fendiline treatment. **D** Representative confocal images from live cell imaging of HEK293 cells expressing GFP-LactC2 and treated with fendiline for 24 hours; scale bars = 10 µm. **E** Effect of fendiline

on PS plasma membrane localization was calculated by the ratio of GFP fluorescence at the (plasma membrane intensity/intracellular intensity). Values are normalized to DMSO control and are reported as mean ± s.d.; N>15, n=3; A one-way ANOVA was performed with multiple comparisons compared to the DMSO control. **p=0.0045; ***p=0.0003. **f** N&B analysis of HEK293 cells expressing the control GFP. Analysis was performed at 48 hours post treatment (DMSO) to align with N&B analysis performed on experiments with HEK293 cells expressing GFP-LactC2 or GFP-eVP40 and treated with the control or fendiline. *Left panel:* Representative images from time-lapse (30 frames) of HEK293 expressing EGFP and treated with fendiline for 48 hours. scale bar = 5 µm. *Middle panel:* Brightness and Intensity plots for representative image. *Right panel:* Selection map correlating each pixel in the representative image to an oligomerization state (b value) (red: monomer). PS: phosphatidylserine; PA: phosphatidic acid; N&B: number & brightness analysis.

Expanded View 5 (EV5)

Vero E6 toxicity and effect of fendiline on eVP40 plasma membrane localization at 24 hours post treatment. A CellTiter-Glo® viability results of Vero cells. Cells were treated with control or fendiline for 48 hours according to the BSL-4 infection model; d-1/0 (black line), e.d. (blue line) and e.o.d (gray line) and viability was assessed as a % viability of control (n = 3). **B-C** Effect of fendiline on eVP40 PM localization in HEK293 cells after 24 hours of treatment. **B** Representative confocal images from live cell imaging experiments of HEK293 cells expressing EGFP-WT-eVP40 after 48 hours of fendiline treatment. scale bars= 10 µm. **C** Effect of fendiline on eVP40 PM localization was

quantified by the ratio of EGFP fluorescence intensity at the PM / total GFP fluorescence intensity (and normalized to DMSO control). N>15, n=3. Values are reported as mean ± s.d. A one-way ANOVA with multiple comparisons was performed compared to the DMSO control. PM: plasma membrane.

Tables

Table 1. Mathematical model parameter descriptions and values

Symbol	Description	Unit	Value from calibration to budding and entry assays	Ranges based on fits to budding and entry assays	Value from calibration to BSL4 data – using ranges defined by budding and entry assays
β	Infection rate constant of target cells by free virions	$(\text{Virion.day})^{-1}$	N/A	0 - inf	$6.6\text{x}10^{-6}$
δ	Death rate constant of infected cells	Day^{-1}	N/A	0 - inf	$4.6\text{x}10^{-6}$
c	Decay rate constant of free virions	Day^{-1}	N/A	0 - 5	5
p	Viral production rate constant by infected cells	$\text{Virions.(Infected cell.day)}^{-1}$	N/A	1 - inf	49
H_b	Hill constant for Fendiline effects on VLP budding		2.7	0.5 - 7	3.4
H_e	Hill constant for Fendiline effects on VLP entry		11	0.5 - 20	4.7

C_{50}^{b}	Concentration with 50% of maximum Fendiline effect on VLP budding	μM	5.7	2 - 20	18
C_{50}^{e}	Concentration with 50% of maximum Fendiline effect on VLP entry	μM	4.8	0.5 - 20	15
E_{max}^{b}	Maximum Fendiline effect on VLP budding		0.98	0.3 - 1	0.3
E_{max}^{e}	Maximum Fendiline effect on VLP entry		0.76	0.3 - 1	0.33

Table 2. Antibodies used in immunoblotting

Target	Species	Tag	Dilution	Cat. #	Source
eVP40	Rabbit		1/40,000	0301-010	IBT Bioservices
Rabbit	Goat	HRP	1/5,000	205718	Abcam
GAPDH	Mouse		1/5,000	8245	Abcam
Mouse	Sheep	HRP	1/10,000	6808	Abcam
EBOV-GP (KZ52)	Human		1.0 µg/ml	0260-001	IBT Bioservices
Human	Goat	Alexa-488	0.7 µg/ml	A11013	Invitrogen
Mouse	Goat	Alexa-488	1.0 µg/ml	A11029	Invitrogen
6xHis	Mouse		1/1,000	A5588	Sigma

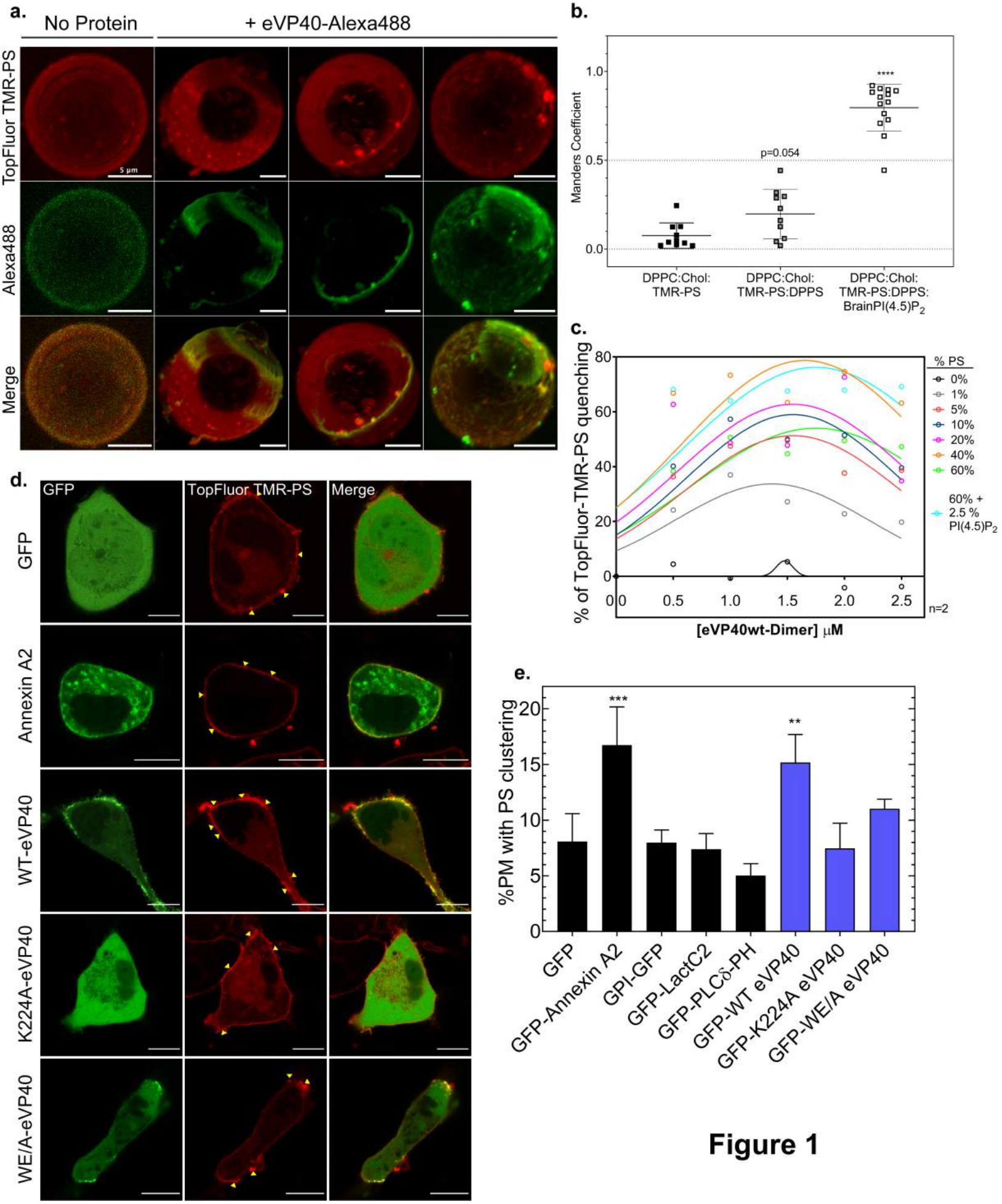
a.
No Protein
+ eVP40-Alexa488
TopFluor TMR-PS
Alexa488
Merge
5 µm
b.
Manders Coefficient
1.0
0.5
0.0
****
p=0.054
DPPC:Chol: TMR-PS
DPPC:Chol: TMR-PS:DPPS
DPPC:Chol: TMR-PS:DPPS: BrainPI(4.5)P2
c.
% of TopFluor-TMR-PS quenching
80
60
40
20
0
0.0
0.5
1.0
1.5
2.0
2.5
[eVP40wt-Dimer] µM
n=2
% PS
0%
1%
5%
10%
20%
40%
60%
60% + 2.5 % PI(4.5)P2
d.
GFP
TopFluor TMR-PS
Merge
GFP
Annexin A2
WT-eVP40
K224A-eVP40
WE/A-eVP40
e.
%PM with PS clustering
20
15
10
5
0
***
**
GFP
GFP-Annexin A2
GPI-GFP
GFP-LactC2
GFP-PLCδ-PH
GFP-WT eVP40
GFP-K224A eVP40
GFP-WE/A eVP40

Figure 1

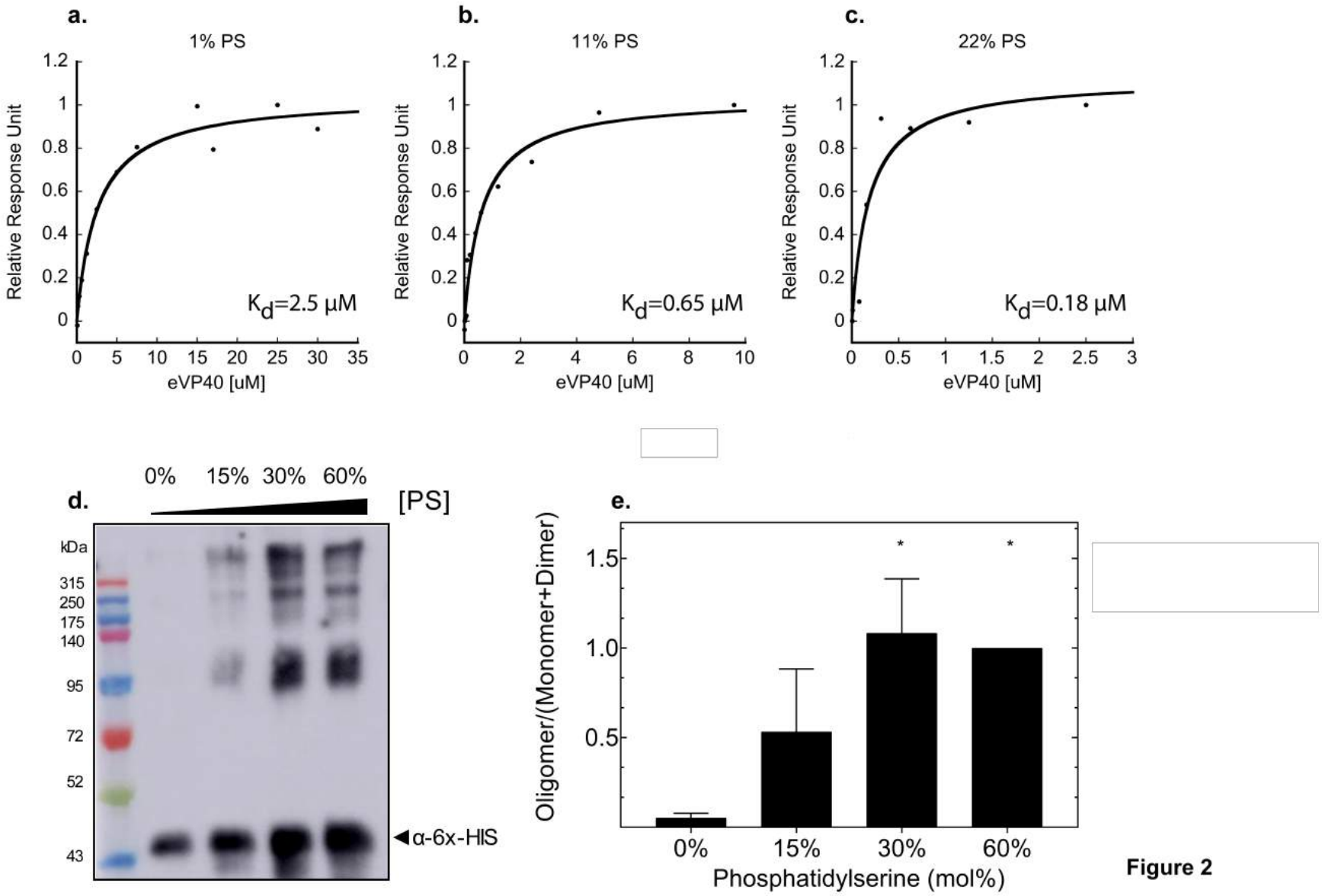
a.
1% PS
Relative Response Unit
eVP40 [uM]
K_d=2.5 μM
b.
11% PS
Relative Response Unit
eVP40 [uM]
K_d=0.65 μM
c.
22% PS
Relative Response Unit
eVP40 [uM]
K_d=0.18 μM
d.
0%
15%
30%
60%
[PS]
kDa
315
250
175
140
95
72
52
43
α-6x-HIS
e.
Oligomer/(Monomer+Dimer)
0%
15%
30%
60%
Phosphatidylserine (mol%)

Figure 2

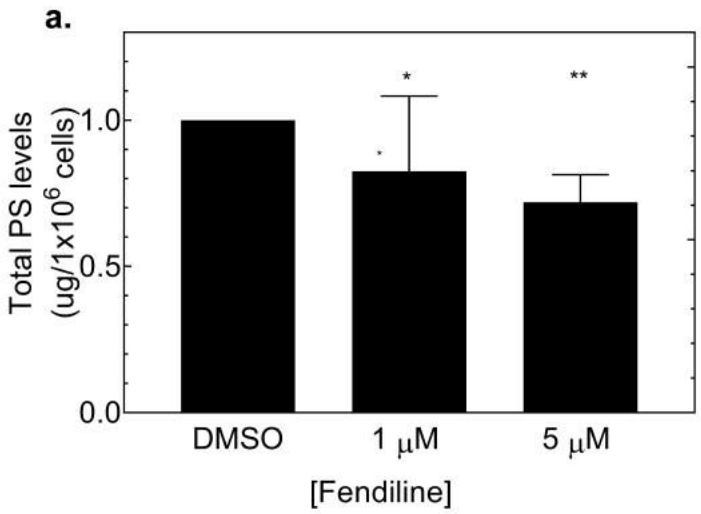
a.
Total PS levels (ug/1x10^6 cells)
1.0
0.5
0.0
*
**
DMSO
1 μM
5 μM
[Fendiline]

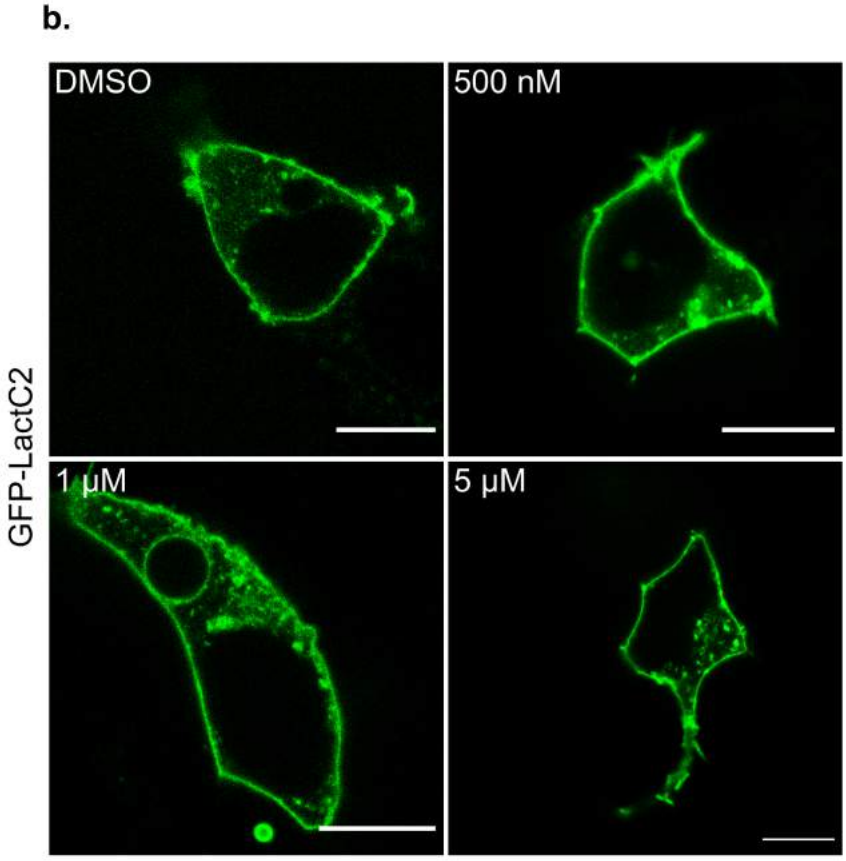
b.
DMSO
500 nM
1 μM
5 μM
GFP-LactC2

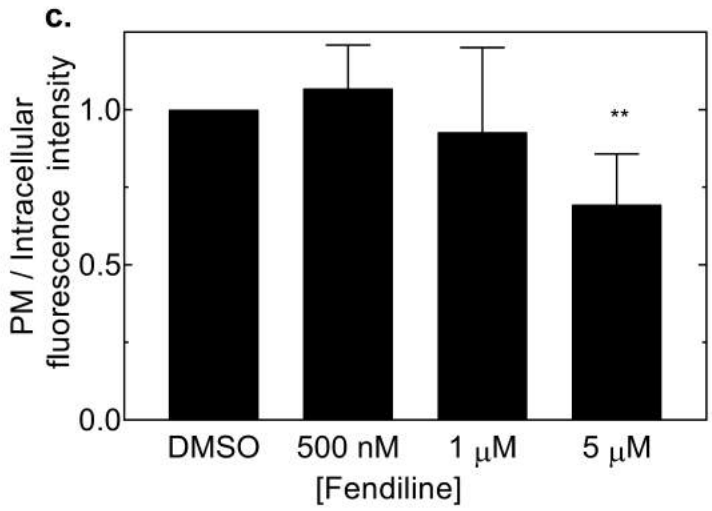
c.
PM / Intracellular fluorescence intensity
1.0
0.5
0.0
**
DMSO
500 nM
1 μM
5 μM
[Fendiline]

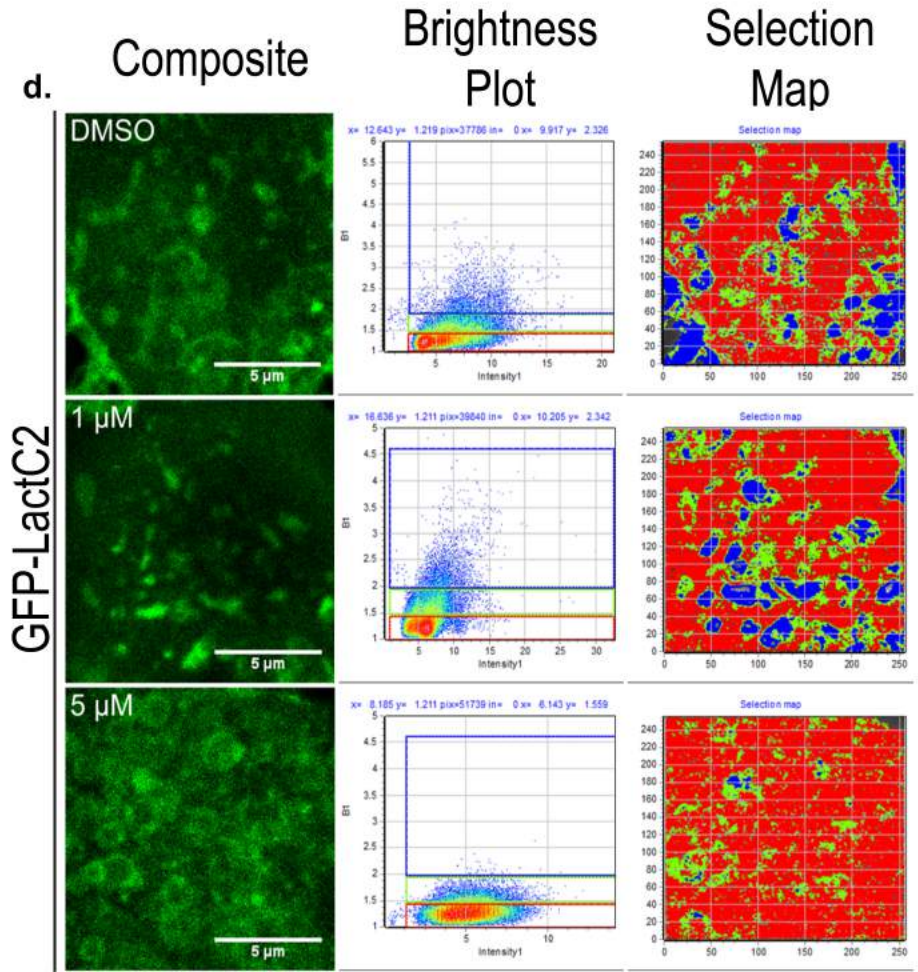
d.
Composite
Brightness Plot
Selection Map
GFP-LactC2
DMSO
1 μM
5 μM
5 μm
Selection map
Intensity1

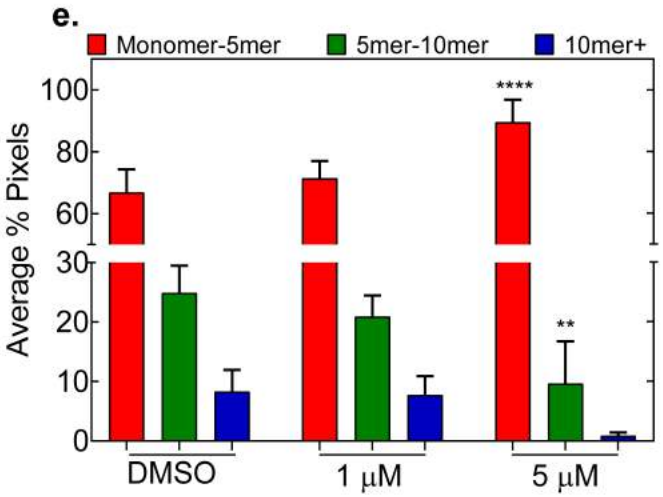
e.
Monomer-5mer
5mer-10mer
10mer+
Average % Pixels
100
80
60
30
20
10
0
****
**
DMSO
1 μM
5 μM

Figure 3

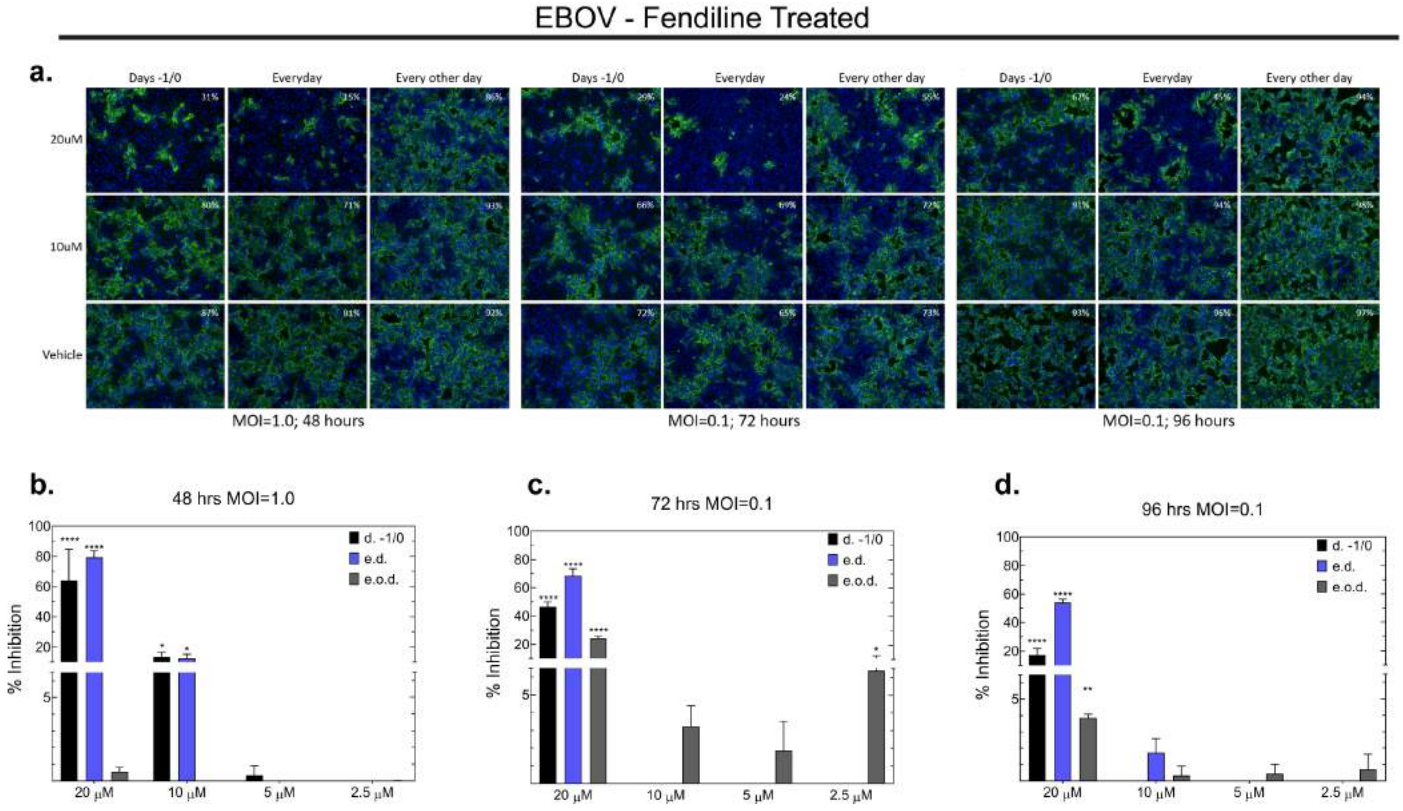
EBOV - Fendiline Treated
a.
Days -1/0
Everyday
Every other day
20uM
10uM
Vehicle
MOI=1.0; 48 hours
MOI=0.1; 72 hours
MOI=0.1; 96 hours
b.
48 hrs MOI=1.0
c.
72 hrs MOI=0.1
d.
96 hrs MOI=0.1
% Inhibition
d. -1/0
e.d.
e.o.d.
20 μM
10 μM
5 μM
2.5 μM

Figure 4

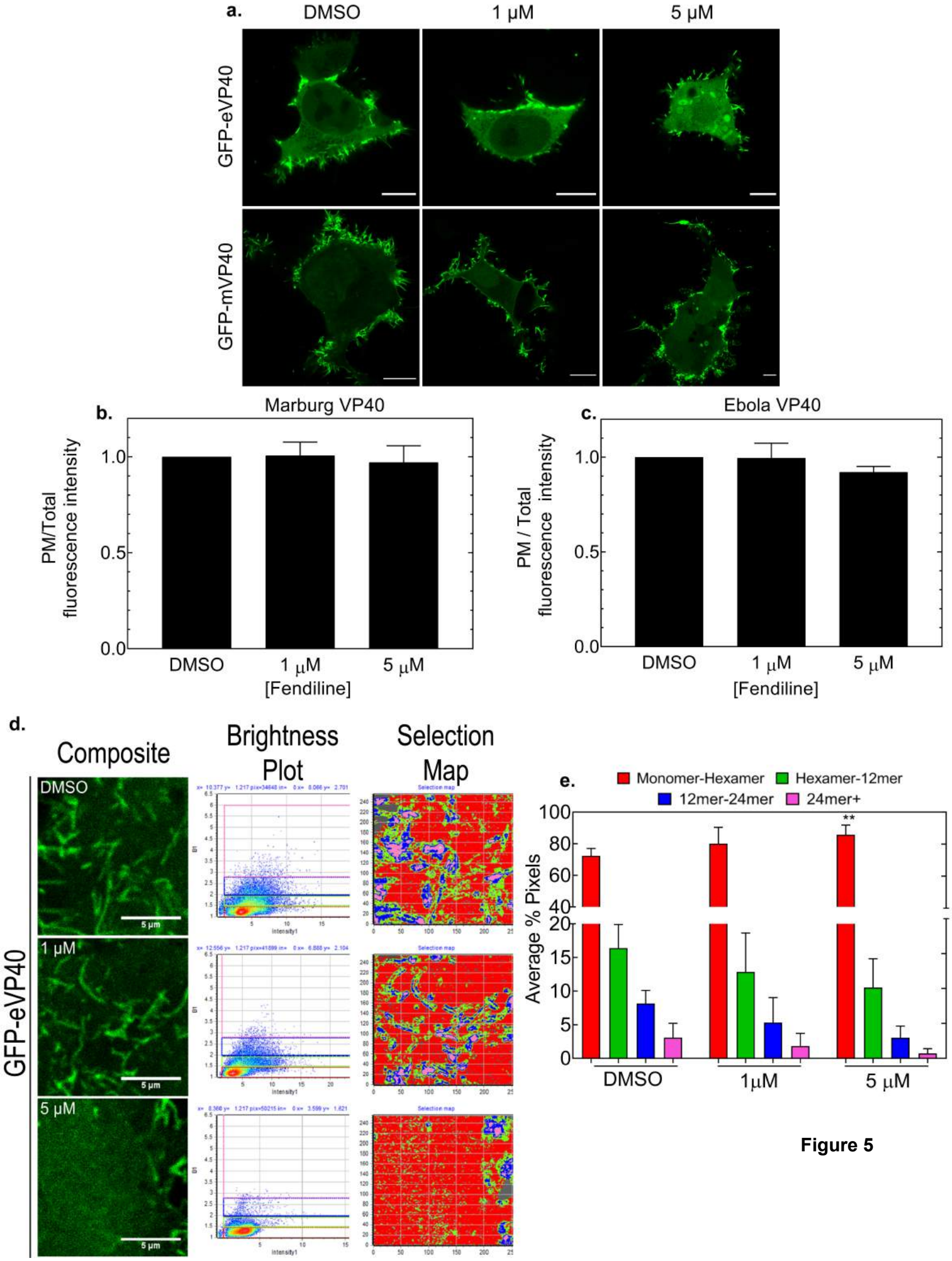
a.
DMSO
1 μM
5 μM
GFP-eVP40
GFP-mVP40
b.
Marburg VP40
PM/Total fluorescence intensity
1.0
0.5
0.0
DMSO
1 μM
5 μM
[Fendiline]
c.
Ebola VP40
PM / Total fluorescence intensity
1.0
0.5
0.0
DMSO
1 μM
5 μM
[Fendiline]
d.
Composite
Brightness Plot
Selection Map
GFP-eVP40
DMSO
1 μM
5 μM
5 μm
e.
Monomer-Hexamer
Hexamer-12mer
12mer-24mer
24mer+
Average % Pixels
100
80
60
40
20
15
10
5
0
**
DMSO
1μM
5 μM

Figure 5

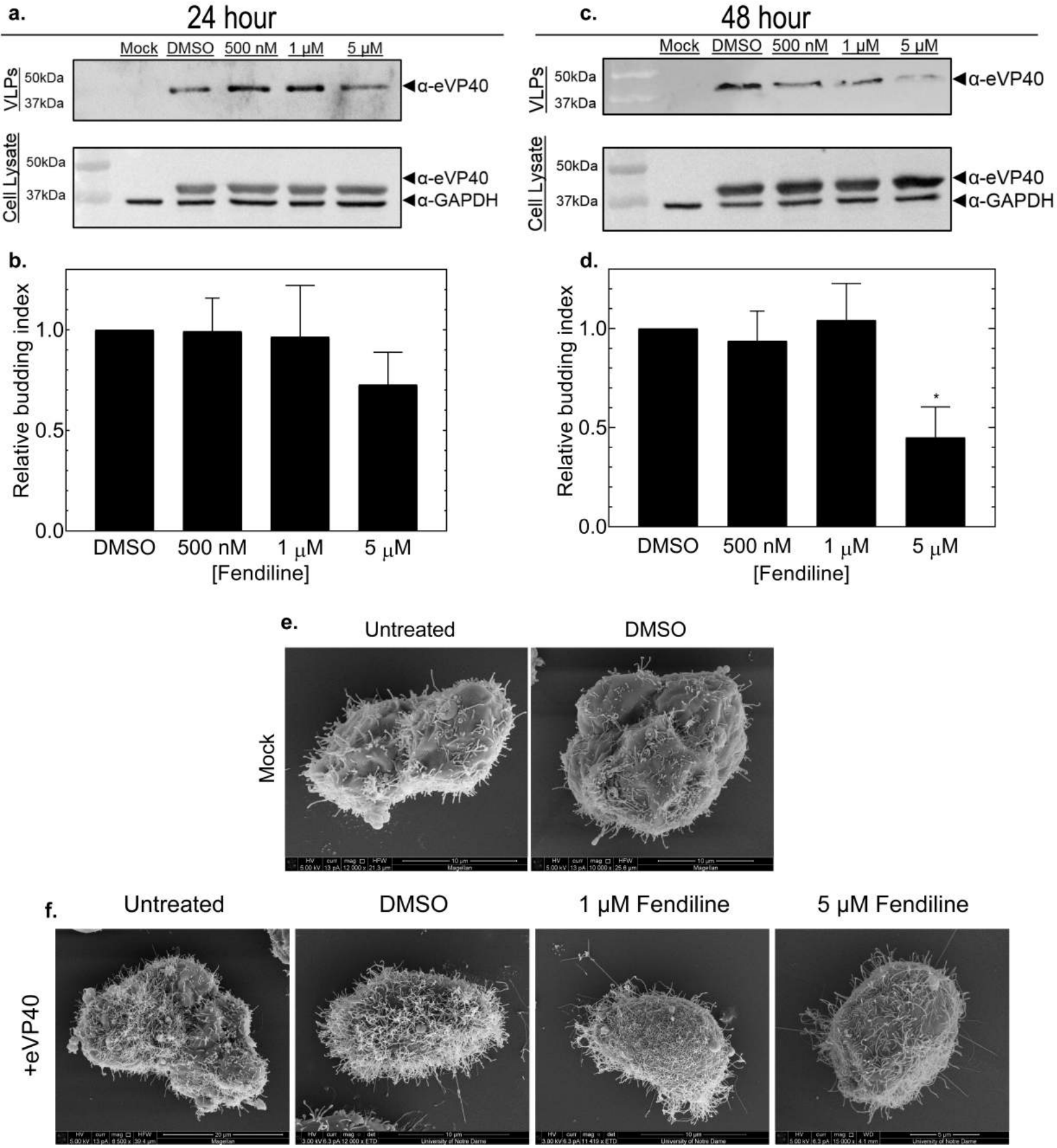
a.
24 hour
Mock
DMSO
500 nM
1 μM
5 μM
VLPs
50kDa
37kDa
α-eVP40
Cell Lysate
50kDa
37kDa
α-eVP40
α-GAPDH
c.
48 hour
Mock
DMSO
500 nM
1 μM
5 μM
VLPs
50kDa
37kDa
α-eVP40
Cell Lysate
50kDa
37kDa
α-eVP40
α-GAPDH
b.
Relative budding index
1.0
0.5
0.0
DMSO
500 nM
1 μM
5 μM
[Fendiline]
d.
Relative budding index
1.0
0.5
0.0
*
DMSO
500 nM
1 μM
5 μM
[Fendiline]
e.
Untreated
DMSO
Mock
f.
Untreated
DMSO
1 μM Fendiline
5 μM Fendiline
+eVP40

Figure 6

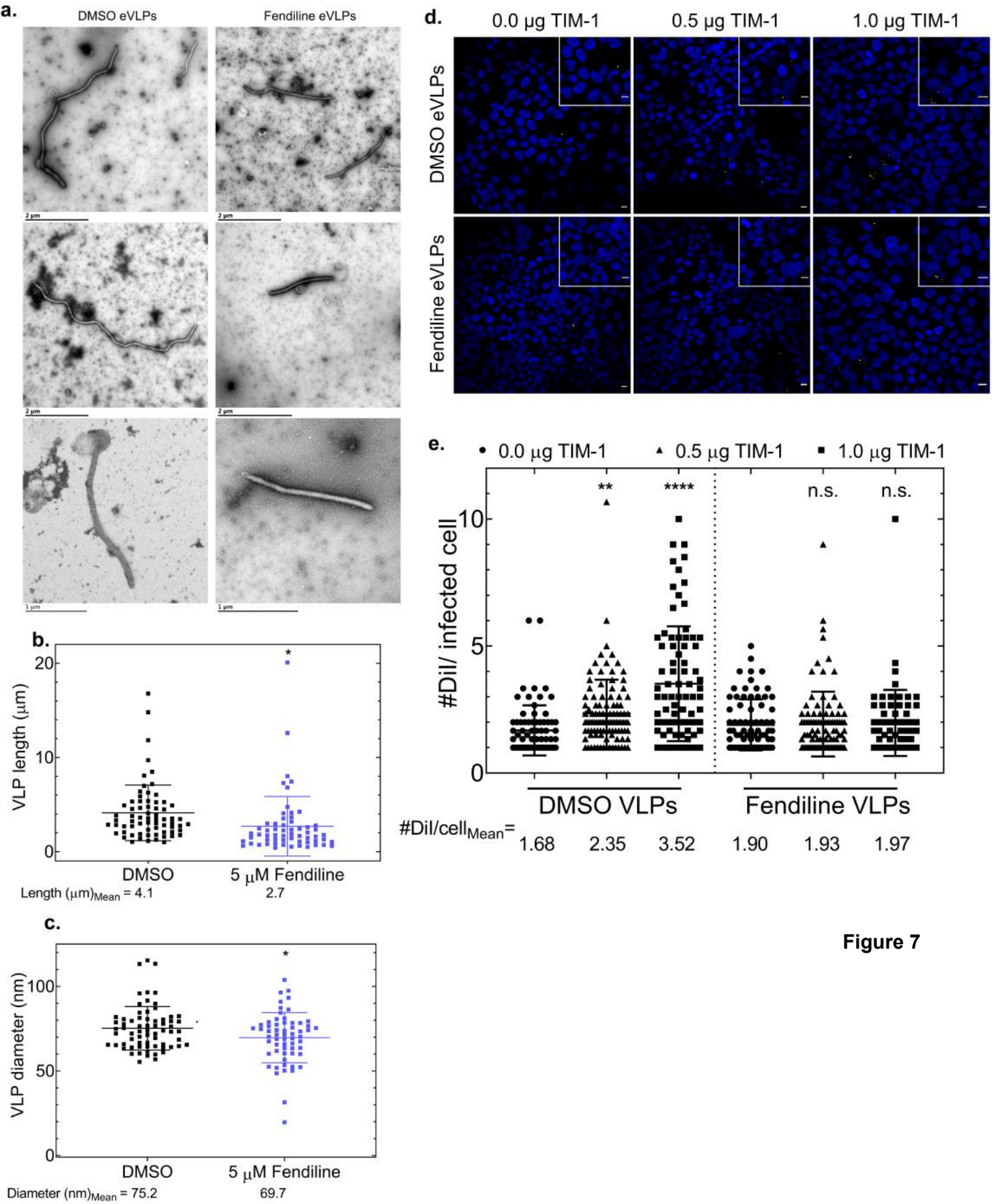
a.
DMSO eVLPs
Fendiline eVLPs
2 µm
1 µm
b.
VLP length (µm)
20
10
0
*
DMSO
5 µM Fendiline
Length (µm)Mean = 4.1
2.7
c.
VLP diameter (nm)
100
50
0
*
DMSO
5 µM Fendiline
Diameter (nm)Mean = 75.2
69.7
d.
0.0 µg TIM-1
0.5 µg TIM-1
1.0 µg TIM-1
DMSO eVLPs
Fendiline eVLPs
e.
0.0 µg TIM-1
0.5 µg TIM-1
1.0 µg TIM-1
#DiI/ infected cell
10
5
0
**
****
n.s.
n.s.
DMSO VLPs
Fendiline VLPs
#DiI/cellMean=
1.68
2.35
3.52
1.90
1.93
1.97

Figure 7

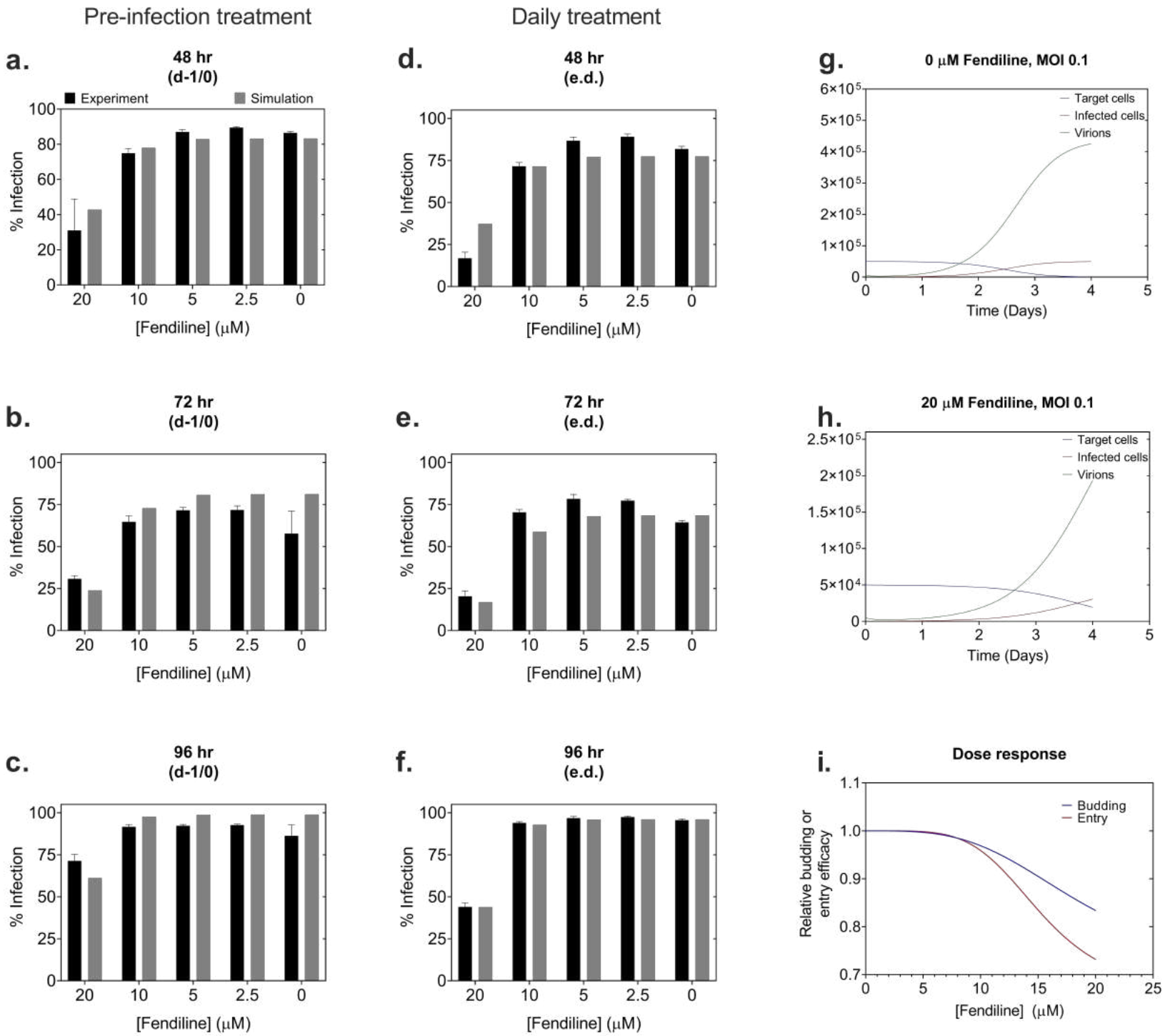
Pre-infection treatment
Daily treatment
a.
48 hr
(d-1/0)
Experiment
Simulation
% Infection
[Fendiline] (μM)
b.
72 hr
(d-1/0)
c.
96 hr
(d-1/0)
d.
48 hr
(e.d.)
e.
72 hr
(e.d.)
f.
96 hr
(e.d.)
g.
0 μM Fendiline, MOI 0.1
Target cells
Infected cells
Virions
Time (Days)
h.
20 μM Fendiline, MOI 0.1
i.
Dose response
Budding
Entry
Relative budding or entry efficacy

Figure 8

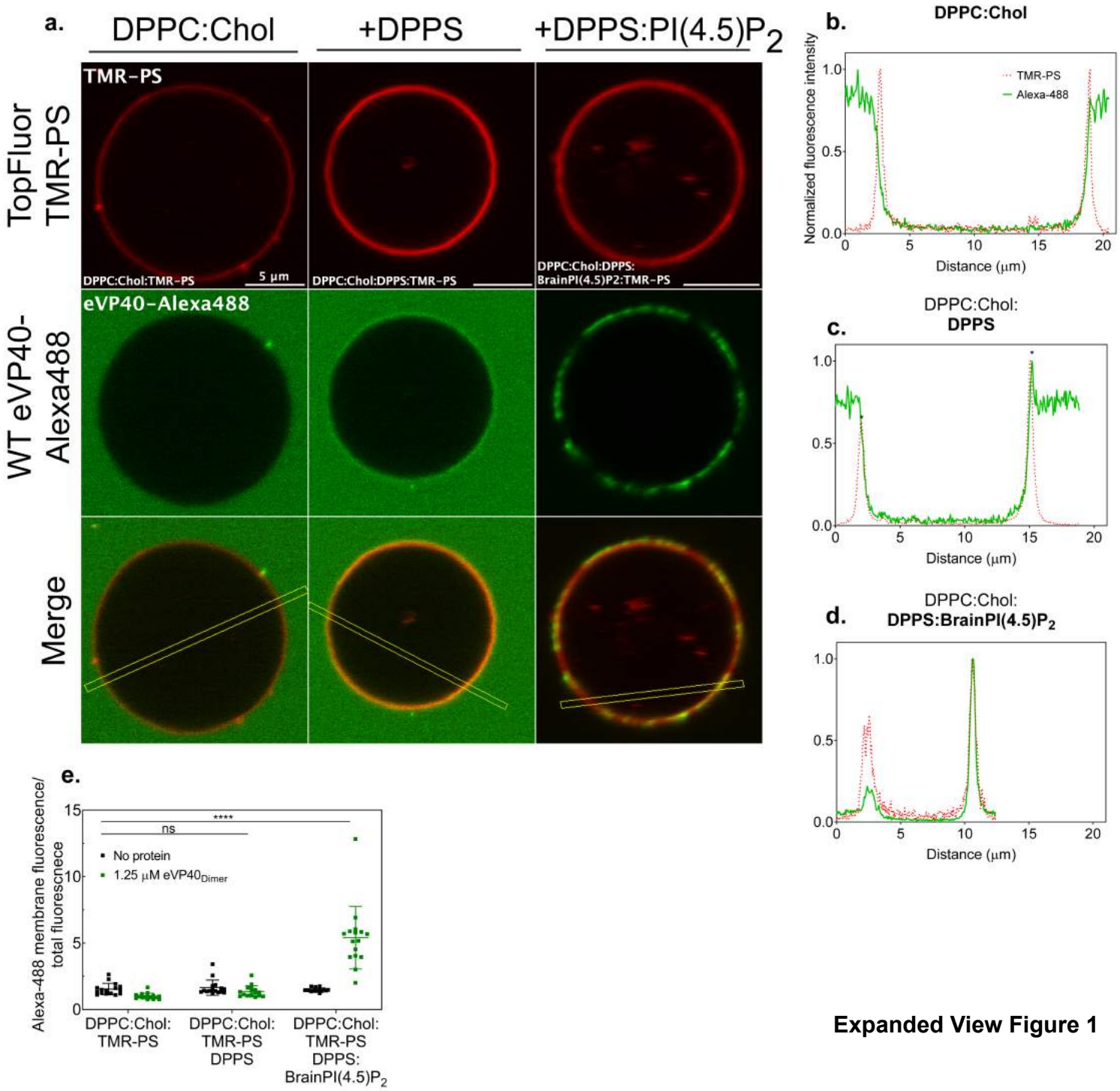

Expanded View Figure 1

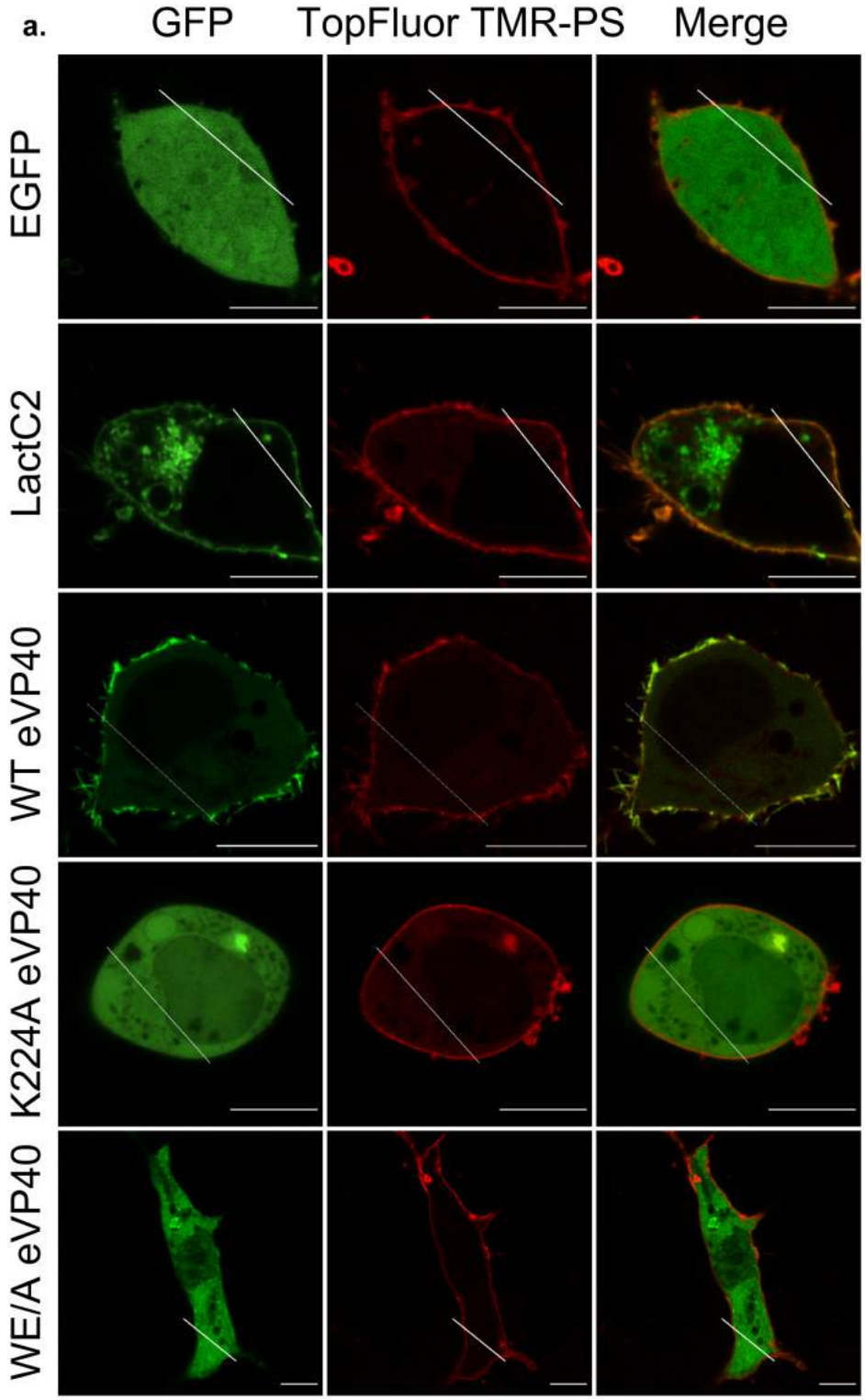

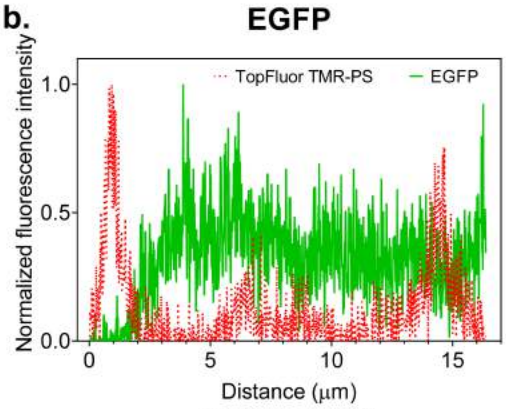

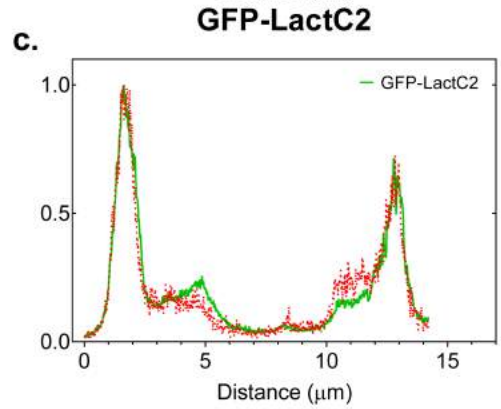

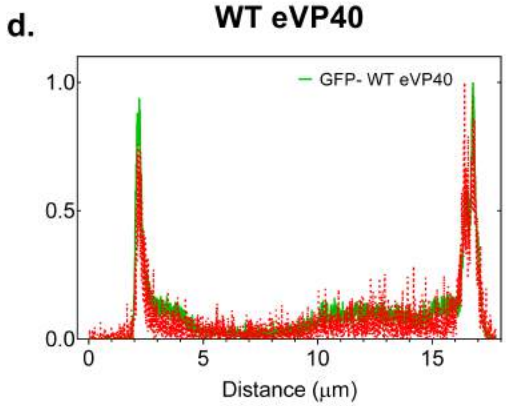

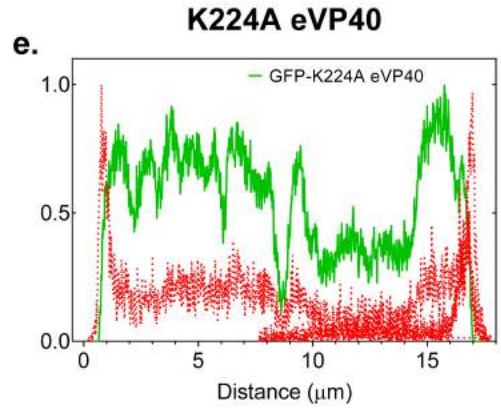

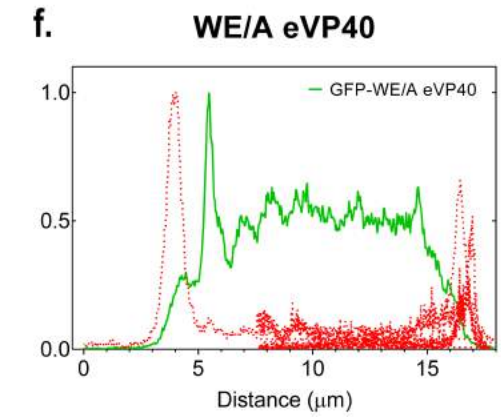

Expanded View Figure2

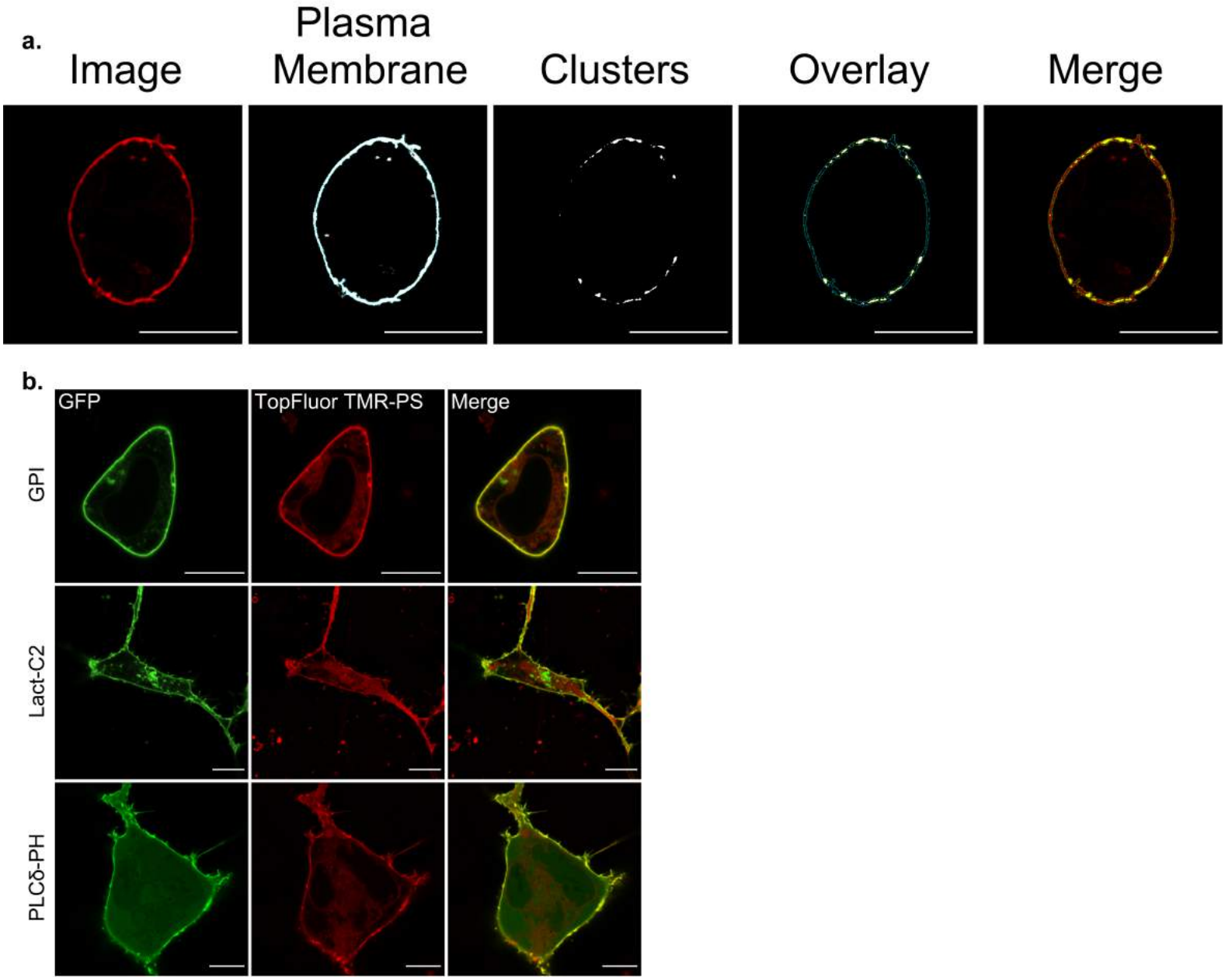

Expanded View Figure 3

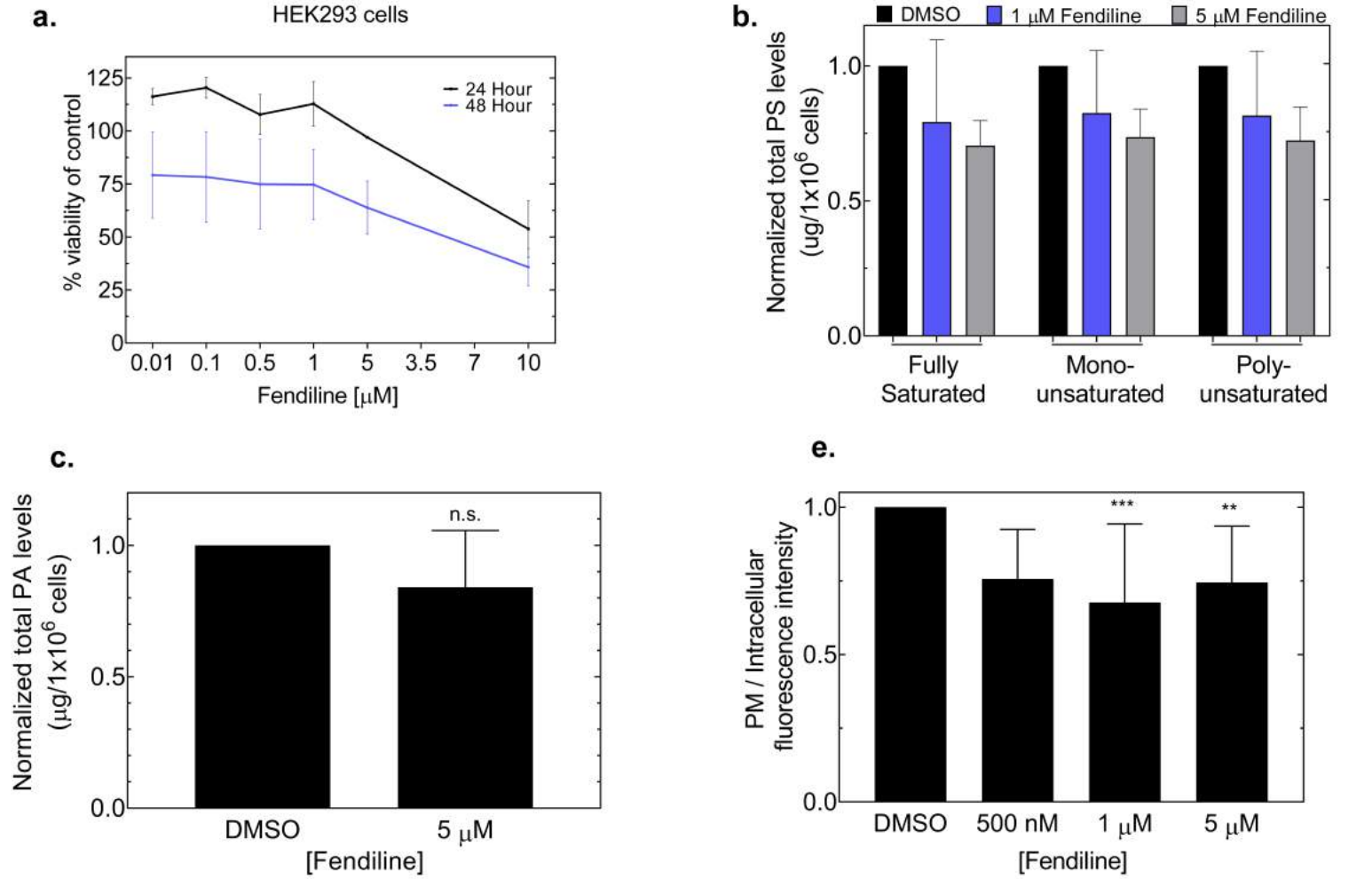

Expanded View Figure 4

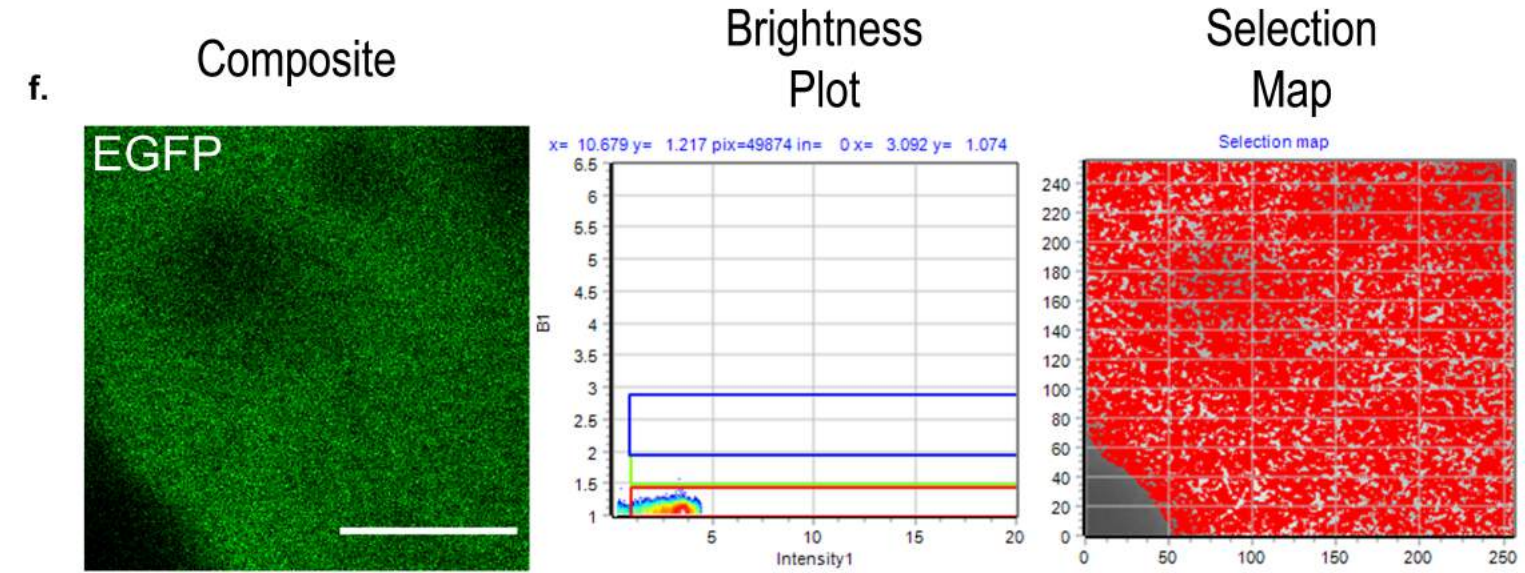

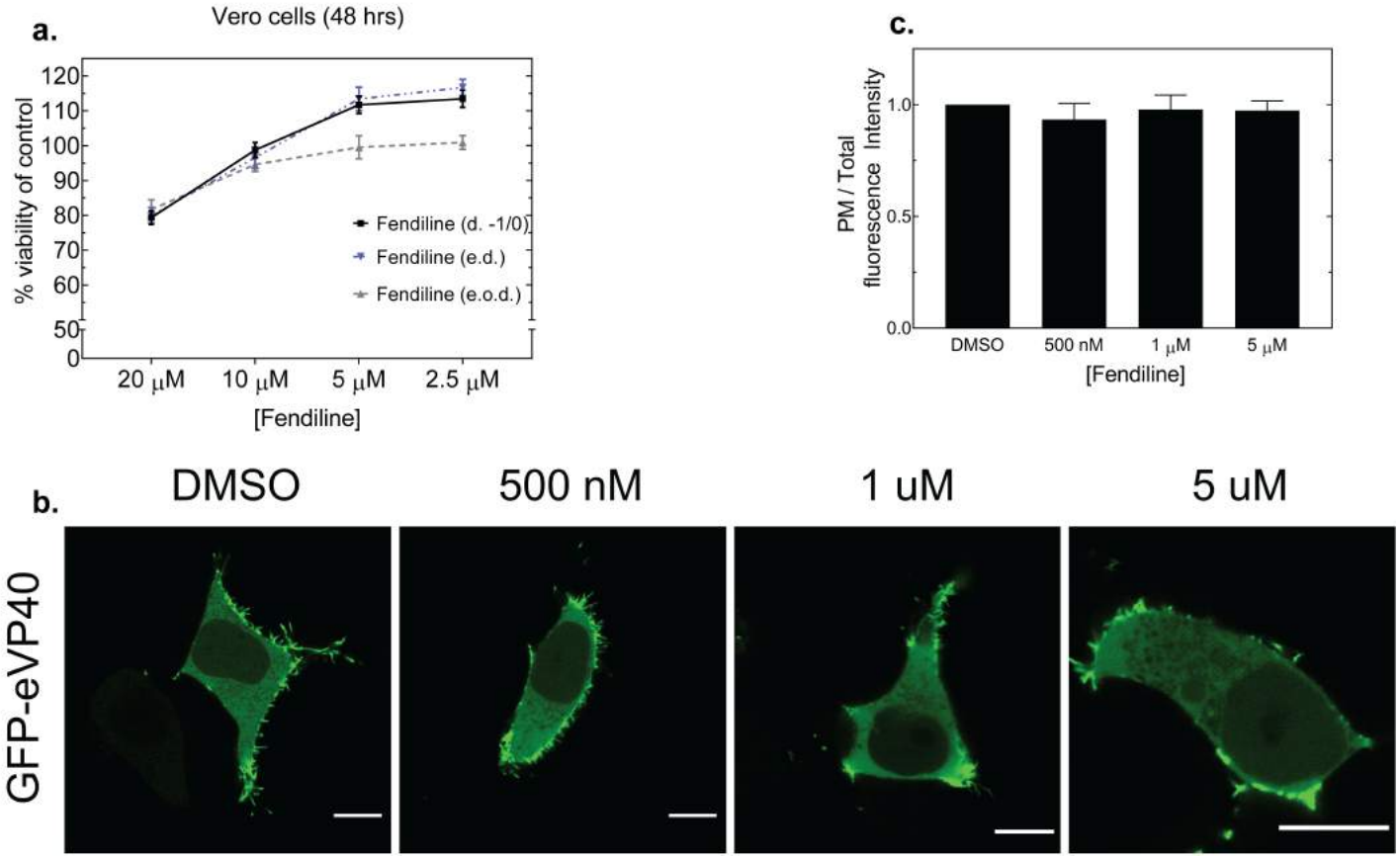

Expanded View Figure 5